International Journal of Multiphase Flow 146 (2022) 103865

Contents lists available at ScienceDirect

International Journal of Multiphase Flow

journal homepage: www.elsevier.com/locate/ijmulflow

Large-eddy simulation of cavitation inception in a shear flow

Filipe L. Brandao, Krishnan Mahesh *

University of Minnesota, Aerospace Engineering & Mechanics, USA

ARTICLE INFO

Keywords:
Large eddy simulation
Inception
Shear layer

ABSTRACT

We present a numerical study of inception in the shear layer of a backward-facing step under the same conditions as experiments (Agarwal et al., 2018). The velocity field is shown to be in good agreement with experiments. Since inception is a stochastic process that generates small amounts of vapor for short periods of time, the effects of these small regions of vapor on the liquid density and dynamics can be neglected. Vapor is therefore treated as a passive scalar in an incompressible liquid and modeled using the same vapor transport equation as that in a fully compressible homogeneous mixture model. The model is validated against the compressible homogeneous mixture approach at incipient conditions. Both velocity and scalar fields are advanced using the implicit Crank–Nicolson scheme. However, the scalar field is solved in an inner loop at a smaller time step than the velocity field. Statistics are computed for both pressure and vapor volume fraction, and the likelihood of inception is determined. The locations of the preferred sites for cavitation are compared to experimental results and good agreement is achieved. The effects of finite rate evaporation and condensation are revealed by the probability density functions of pressure and volume fraction. The flow topology is investigated and inception is found to occur in the core of the stretched tubular vortical structures with a rotation rate four times higher than the stretching rate. These cavitating tubular structures are elongated two to three times more in their most extensive principal direction than in their intermediate principal direction, and are most likely aligned with the streamwise direction. Decreasing the cavitation number from 0.55 to 0.45 is found to drop the minimum pressure inside the vortices from −1500 Pa to −5500 Pa and increase the cavitation event rates by around $O(1)$.

1. Introduction

Cavitation is the process of vapor formation due to a drop in pressure. It is usually triggered by imperfections in water that are often very small vapor bubbles known as nuclei that serve as the starting point for the liquid breakdown. This phenomenon can occur at different scales, starting from inception and ending in developed cavitation, and are characterized by the cavitation number σ (defined as $\sigma = \frac{p_r - p_v}{0.5\rho u_r^2}$, where p_r, p_v, ρ and u_r are a reference pressure, the vapor pressure, the liquid density and a reference velocity, respectively). Inception, being the first stage, is defined by small amounts of vapor production for brief periods at a relative high σ. It is commonly observed in the turbulent shear layers, tip vortices and wakes of marine geometries (e.g. hydrofoils, propeller blades, etc.), where the pressure fluctuations can be extreme. Consequently, shear flows are often more prone to cavitation than streamlined bodies, resulting in considerably higher inception σ. Cavitating shear flows have been investigated in the past. Katz and O'Hern (1986) observed that the first traces of cavitation appear as a series of narrow and long axial structures located between spanwise eddies. This was later confirmed in O'Hern (1990), where the incipient streamwise vortices showed a strength less than 10% of that of the spanwise vortices. Interestingly, Iyer and Ceccio (2002) noticed that cavitation does not significantly alter the overall formation, growth and convection of the primary and secondary vortices. The same behavior was observed later by Aeschlimann and Barre (2009), but the reattachment point was found to depend on σ. Studies conducted by Agarwal et al. (2018) revealed that regions most likely to cavitate move upstream with decreasing σ and increasing velocity. The work of Agarwal et al. (2020) showed that the Reynolds number ($Re = u_r L_r/\nu$, where L_r and ν are a reference length and the kinematic viscosity respectively) has a strong influence on the time the pressure remains below vapor pressure inside the streamwise vortices.

The inception regime is difficult to predict. Experimentally, inception can be determined through visual or acoustical techniques where the measurements detect events per unit time above a certain threshold (Rood, 1991). Numerous factors can affect the conditions for inception. As observed by Katz and O'Hern (1986), Arndt et al. (1991) and Khoo et al. (2020), the cavitation number associated with the appearance of inception has a strong dependence on the air content

* Corresponding author.
E-mail address: kmahesh@umn.edu (K. Mahesh).

https://doi.org/10.1016/j.ijmultiphaseflow.2021.103865
Received 9 April 2021; Received in revised form 13 September 2021; Accepted 13 October 2021
Available online 23 October 2021

of the fluid and the population of bubbles in the freestream. Arndt and Keller (1992), through visual detection, observed that inception in tip vortices would start at higher σ for "weak" water (water where the tensile strength was reduced by the presence of bubbles) and that it was highly intermittent, as opposed to the sudden appearance of a well defined cavitating structure for the "strong" water. The decrease in the inception σ can be approximately 60% with increasing water tension for tip vortex cavitation (Gindroz and Billet, 1998). Besides, Peterson (1972) found a disagreement between the determination of inception using visual and acoustical measurements in a water tunnel with large nuclei concentration. Interestingly, Khoo et al. (2020) found that the desinence of cavitation (disappearance of cavitation by slowly increasing σ) is largely independent of the nuclei population.

Inception is commonly simulated using an Euler–Lagrange framework, where the liquid follows the incompressible Navier–Stokes equations and each bubble is tracked individually with the equations of motion coupled with the Rayleigh–Plesset equation for their size (Farrel, 2003; Hsiao et al., 2003; Hsiao and Chahine, 2005; Shams et al., 2011). For a more developed cavitation, usually a compressible formulation using the homogeneous mixture approach is preferred (Gnanaskandan and Mahesh, 2015; Egerer et al., 2016; Budich et al., 2018; Bhatt and Mahesh, 2020; Brandao et al., 2020). The difference in approaches is due to the distinct characteristics of both regimes. For developed cavitation, the presence of regions with large amounts of vapor can make the flow locally supersonic. This can lead to the formation of shock waves and the use of a compressible formulation for the equations becomes more appropriate. For inception however, the use of the compressible equations can be very expensive. This is because numerically capturing inception requires very low values of freestream volume fraction (Bhatt and Mahesh, 2021). This increases the speed of sound in the mixture and the stiffness of the system of equations.

It was previously observed by Katz (1984), Katz and O'Hern (1986) and O'Hern (1990) that the inception σ typically increases with Reynolds number in shear layers. A larger Re produces a wider frequency spectrum, increasing the likelihood of instantaneous pressure reaching values below vapor pressure (Rood, 1991). Due to this unsteady and statistical nature of inception, LES (Large-Eddy Simulation) is preferred over RANS (Reynolds-Averaged Navier–Stokes) for numerical simulations. Early studies compared the performances between LES and RANS (e.g. Salvatore et al., 2009; Bensow, 2011) for cavitation and concluded that small-scale and transient behaviors are better captured by LES. In flow over propeller blades, for instance, Lu et al. (2012) observed that RANS is not capable of capturing the tip vortical structures, which is detrimental for predicting inception. In a similar problem, Bappy et al. (2019) showed that the inception σ predicted by LES matches the experimental value, while it is underpredicted by RANS. The use of RANS was also found to predict the low-pressure region farther away from the blade.

In the present paper, we use LES to study inception in the shear layer of the backward-facing step experiments of Agarwal et al. (2018). Most LES of cavitation has been applied to attached or sheet-to-cloud regimes using compressible formulations of the homogeneous mixture equations. The inception regime has received less attention in numerical simulations, despite being important for practical applications. Inception occurs in the regime of low void fractions where the compressible governing equations can be argued to reduce to the zero-Mach equations which imply the use of the incompressible governing equations along with the same vapor volume fraction transport equation as the compressible equations. The paper proposes this approach. Since inception is a stochastic process that generates small amounts of vapor for short periods, the effects of these small regions of vapor on the liquid density and dynamics can be neglected. Therefore, here vapor is treated as a passive scalar in the incompressible liquid. Different time steps are used for time advancement of the vapor and velocity fields; the transport equation for the vapor is solved in an inner loop at a smaller time step than that employed for the momentum equation. This is because scalar fronts are thinner than velocity fronts since they do not have pressure to regulate their thickness. An unsteady sharp front implies higher frequencies and therefore smaller timestep. This approach, developed in the context of passive scalar mixing (Muppidi and Mahesh, 2008) is applied here for cavitation simulations. Special attention is paid to the treatment of the source terms to avoid unbounded solutions. The topology of the LES flow field associated with inception is analyzed using velocity gradient invariants. The paper is organized as follows. Section 2 outlines the equations and the method employed. Section 3 provides validation for the model, problem description, and discussion. A summary in Section 4 concludes the paper. Appendix discusses the treatment of the source terms.

2. Governing equations and numerical method

2.1. Governing equations

The filtered Navier–Stokes equations are

$$\frac{\partial \bar{u}_i}{\partial x_i} = 0 \tag{1}$$

$$\frac{\partial \bar{u}_i}{\partial t} + \frac{\partial \bar{u}_i \bar{u}_j}{\partial x_j} = -\frac{\partial \bar{p}}{\partial x_i} + \nu \frac{\partial^2 \bar{u}_i}{\partial x_j \partial x_j} - \frac{\partial \tau_{ij}}{\partial x_j}, \tag{2}$$

where $\tau_{ij} = \overline{u_i u_j} - \bar{u}_i \bar{u}_j$ is the sub-grid scale (SGS) stress and is modeled using the dynamic Smagorinsky eddy-viscosity model (Germano et al., 1991). The filtered transport equation for the vapor is given by:

$$\begin{aligned} \frac{\partial \bar{C}}{\partial t} + \frac{\partial \bar{C}\bar{u}_j}{\partial x_j} - \frac{\nu}{Sc}\frac{\partial^2 \bar{C}}{\partial x_j x_j} + \frac{\partial \tau_s}{\partial x_j} &= \bar{S}_e - \bar{S}_c \\ \bar{S}_e = C_e \bar{\alpha}^2 (1-\bar{\alpha})^2 \frac{\rho_l}{\rho_v} \frac{max(p_v - \bar{p}, 0)}{\sqrt{2\pi R_v T}} \\ \bar{S}_c = C_c \bar{\alpha}^2 (1-\bar{\alpha})^2 \frac{max(\bar{p} - p_v, 0)}{\sqrt{2\pi R_v T}}. \end{aligned} \tag{3}$$

Here, the passive scalar is considered as the concentration of vapor, $C = \rho_v \alpha$, $\bar{()}$ denotes spatial filtering at the filter width Δ, and the cavitation source and sink terms are obtained from Saito et al. (2007). The Schmidt number for vapor in water is taken as $Sc = 500$. The vapor volume fraction is indicated by α and ρ_v is the vapor density, which can be assumed to be constant or to follow the ideal gas law. For the SGS scalar flux, $\tau_s = \overline{Cu}_j - \bar{C}\bar{u}_j$, the dynamic Smagorinsky eddy-diffusivity model (Moin et al., 1991) is employed. The vapor pressure is taken as a function of temperature as

$$p_v = p_k exp\left(\left(1 - \frac{T_k}{T}\right)(a + (b - cT)(T - d)^2)\right) \tag{4}$$

where $p_k = 22.130$ MPa, $T_k = 647.31K$, $a = 7.21$, $b = 1.152 \times 10^{-5}$, $c = -4.787 \times 10^{-9}$ and $d = 483.16$. Brandao et al. (2020) show that this expression provides very good agreement with data from the National Institute of Standards and Technology (NIST). In the source terms, the empirical constants C_e and C_c have units of m^{-1} as given in Saito et al. (2007), and $R_v = 461.6$ J/kgK.

2.2. Numerical method

If Eq. (3) is written in non-dimensional form, the diffusive term becomes $\frac{1}{ReSc}\frac{\partial^2 \tilde{C}}{\partial \tilde{x}_j \tilde{x}_j}$, where the tilde symbol (~) indicates non-dimensional units. This reveals that the diffusion term for the vapor concentration is very small, even for cases at a relatively small Re, and is not enough to smoothen the sharp gradients that may arise in the solution. Thus, the scalar field requires a smaller time step than the velocity field. Therefore, in this work we use an algorithm based on the work of Muppidi and Mahesh (2008) for passive scalar in jets and is outlined as follows: The incompressible Navier–Stokes equations are solved using a predictor–corrector algorithm developed in Mahesh et al. (2004) with Crank–Nicolson scheme for implicit time advancement.

After the velocity and pressure fields are obtained at the new time instance $t^{n+1} = t^n + \Delta t_m$, the passive scalar equation is solved in an inner loop with m smaller time steps using $\Delta t_s = \Delta t_m/m$. The velocity and pressure field at the previous (t^n) and new time instances (t^{n+1}) are interpolated to obtain the convective and diffusive fluxes, as well as the source term at the inner time instance. For the time advancement of the scalar equation, we use the implicit Crank–Nicolson scheme, while the convective fluxes are computed using an upwind discretization. It is relevant to mention that lowering the time step for both scalar and velocity fields would make the simulation more computationally expensive, since the time advancement of the velocity field involves a predictor–corrector method. When our method is compared against the existing numerical approaches for cavitation inception, decoupling the time step used for the scalar field from the one used for the velocity field offers the clear advantage of reducing computational costs.

The algorithm can be summarized as follows.

- Advance u^n and p^n to u^{n+1} and p^{n+1}
  - Use u^n and p^n to advance C^n to $C^{n,1}$
    1. Interpolate: $u^{n,1} = u^n + \frac{u^{n+1}-u^n}{\Delta t_m}\Delta t_s$
    2. Interpolate: $p^{n,1} = p^n + \frac{p^{n+1}-p^n}{\Delta t_m}\Delta t_s$
  - Use $u^{n,1}$ and $p^{n,1}$ to advance $C^{n,1}$ to $C^{n,2}$
    1. Interpolate: $u^{n,2} = u^{n,1} + \frac{u^{n+1}-u^n}{\Delta t_m}\Delta t_s$
    2. Interpolate: $p^{n,2} = p^{n,1} + \frac{p^{n+1}-p^n}{\Delta t_m}\Delta t_s$

    ⋮
  - Use $u^{n,m-1}$ and $p^{n,m-1}$ to advance $C^{n,m-1}$ to C^{n+1}
- Advance u^{n+1} and p^{n+1} to u^{n+2} and p^{n+2}

The unfiltered version of Eq. (3) can be written in the discrete form as

$$V_{cv}\left(\frac{\partial C}{\partial t}\right)_{cv} + \sum_f \left(CV_n\right)_f A_f - \frac{\nu}{Sc}\sum_f \left(\frac{\partial C}{\partial n}\right)_f A_f = V_{cv}\left(S_e - S_c\right), \quad (5)$$

where V_{cv} and A_f represent the volume of a mesh element and the area of a face, respectively. The fluid velocity at a face center and in a direction normal to it is indicated by V_n. To solve Eq. (5), the values of the scalar flux across a face, $(CV_n)_f$, and the face-normal derivative, $\left(\frac{\partial C}{\partial n}\right)_f$, are required. Consider a uniform and structured mesh element, as displayed in Fig. 1(a), where the fluid is moving from $icv1$ to $icv2$. The convective flux at ifa, in an upwind discretization, is computed as

$$(CV_n)_{ifa} = C_{icv1} V_n, \quad (6)$$

and the face-normal derivative can be computed as

$$\left(\frac{\partial C}{\partial n}\right)_{ifa} = \frac{C_{icv2} - C_{icv1}}{d_{icv}}, \quad (7)$$

where d_{icv} is the distance along the solid line connecting $icv1$ and $icv2$ centroids. Consider now a skewed mesh element as shown in Fig. 1(b). It is noted that the line connecting the centroids of the control volumes adjacent to ifa does not pass through the face center and is at an angle with the face normal. Eqs. (6) and (7) become inaccurate in cases like this. Observe now the points A and B in Fig. 1(b). They are connected by a dashed line that is orthogonal to ifa and passes through the face center. Accurate computation of the fluxes requires obtaining the value of C at these points (C_A, C_B). A reconstruction scheme based on least-squares is used for this purpose (Muppidi and Mahesh, 2008), as follows: Given the coordinates of the face center ($x_{i,ifa}$) and the face normal, the coordinate of any point along the face normal (dashed line) can be computed as

$$x_i = l_i r + x_{i,ifa}, \quad (8)$$

where l_i is the directional cosine of the face normal and r is a length variable. Let r_A be the value of r that minimizes the distance between A and $icv1$ centroid in a least-square sense (e.g. $(x_{i,A} - x_{i,icv1})^2$), and r_B be the value of r that minimizes the distance between B and $icv2$ centroid, also in a least-square sense. The final value for r is the one that minimizes both as $r = min[r_A, r_B]$. With the locations of points A and B in hand, C_A, C_B and the fluxes can be computed as

$$\begin{aligned} C_A &= C_{icv1} + (\nabla C)_{icv1}(x_{i,A} - x_{i,icv1}), \\ (CV_n)_{ifa} &= C_A V_n, \\ \left(\frac{\partial C}{\partial n}\right)_{ifa} &= \frac{C_B - C_A}{d_{AB}}, \end{aligned} \quad (9)$$

where d_{AB} is the distance between points A and B.

3. Results

The presented model is employed to study inception in shear layers using the experimental setup from Agarwal et al. (2018) of a backward-facing step with an inflow turbulent boundary-layer. We simulate the experimental cases of $Re_\tau = \frac{\delta u_\tau}{\nu} = 800$ and 1500 (where δ is the boundary-layer thickness, u_τ is the friction velocity and ν is the kinematic viscosity). The domain has a step height (S) of 10 mm, an expansion ratio (ER) of 1.19 and an aspect ratio (AR) equal to 5.3. A sketch of the domain is shown in Fig. 2. No-slip boundary conditions are applied to every wall in the domain and the outflow is located at $22.8S$ downstream from the step corner. The inflow turbulent boundary-layer is generated through the recycle-rescale method of Lund et al. (1998), later extended to unstructured grids by Kumar and Mahesh (2016). The flow where $Re_\tau = 800$ does not result in inception for any σ considered by Agarwal et al. (2018). Therefore, we simulate $Re_\tau = 800$ at a lower σ to validate the flow field and focus the analysis on the $Re_\tau = 1500$ flow.

We verify that our present model, which combines the incompressible Navier–Stokes equations with a vapor transport equation, agrees with a fully compressible homogeneous mixture model under inception conditions. Towards this end, we perform simulations under inception conditions over a backstep with the same ER and AR as Agarwal et al. (2018) and compare to corresponding results obtained using the fully compressible homogeneous mixture model employing the same source terms from Saito et al. (2007), where acoustic stiffness is handled by the preconditioning methodology developed by Bhatt and Mahesh (2021). In the compressible homogeneous mixture approach, the mixture of water and vapor is considered as a single compressible medium where the phases are at mechanical equilibrium (i.e. each phase has the same pressure as the pressure of the cell and the slip velocity between the phases is neglected) and thermal equilibrium (i.e. temperature of each phase is same as the cell temperature). More details can be found in the works of Gnanaskandan and Mahesh (2015), Bhatt and Mahesh (2020) and Brandao et al. (2020). It is important to point out that in the present study, inception is assumed to have occurred when there are instances of time in which the local pressure anywhere in the domain drops below vapor pressure. The same criteria may not be used in other studies.

3.1. Comparison with homogeneous mixture model

The backstep used in this comparison has the same ER and AR as the configuration of Agarwal et al. (2018). The step height, however, is smaller to result in $Re = \frac{u_\infty S}{\nu} = 200$ with $u_\infty = 10$ m/s. This small value for Re is chosen to make the solution independent of subgrid model. The boundary conditions are the same as those used for the main inception study, except for the inflow which does not have an incoming turbulent boundary-layer. The very low Re used in this comparison results in a two-dimensional flow. Thus, the grid is coarsened to $\Delta x/S = 1$ and $\Delta y/S = 0.1$ with 3 points in the spanwise direction. The objective is to compare the values of volume fraction obtained by the present model to those obtained from the compressible homogeneous mixture approach. The compressible homogeneous mixture approach has been validated for different cavitation regimes (Gnanaskandan and Mahesh,

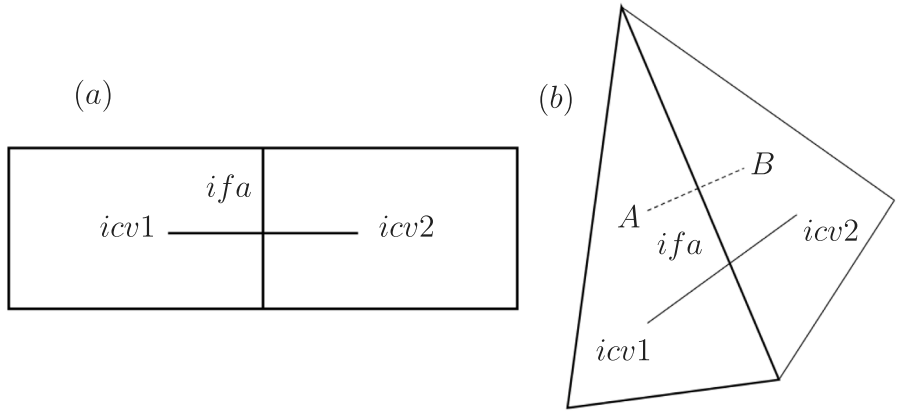

Fig. 1. Examples of a mesh element. An internal face is indicated by ifa and the control volumes adjacent to it are given by $icv1$ and $icv2$.

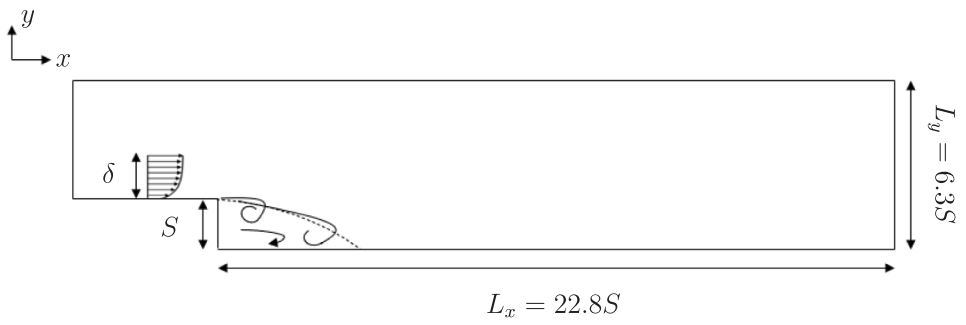

Fig. 2. Computational domain for the backstep problem.

2015; Bhatt and Mahesh, 2020). Therefore, an agreement between volume fraction profiles provides a validation of the present approach. The simulations are performed at $\sigma = 1.98$, based on the inflow pressure and velocity, with a freestream vapor concentration equivalent to a volume fraction of $\alpha = 1{\times}10^{-6}$. It is essential to highlight that the use of a high cavitation number concurrently with a small freestream volume fraction is necessary for such comparison due to two main reasons. The first relates to the fact that, if σ is small to the point of forming considerable amounts of vapor, the flow cannot be deemed divergence-free anymore and the passive scalar assumption fails. The second reason is that when a pocket of vapor collapses, pressure waves are released affecting the flow field, which is not captured by the incompressible Navier–Stokes.

Fig. 3(a), (b) and (c) show profiles of $\langle u\rangle/u_\infty$, $\langle\alpha\rangle$ and $\sqrt{\langle\alpha'^2\rangle}$, respectively, at three different locations downstream of the step. Good agreement is achieved for the mean velocity profiles, showing that the flow dynamics are unaffected by the produced vapor. Profiles of $\langle\alpha\rangle$ and $\sqrt{\langle\alpha'^2\rangle}$ also show very good agreement, indicating that the present method is capable of capturing vapor growth under inception conditions.

3.2. Flow over backstep at $Re_\tau = 800$

The $Re_\tau = 800$ case is simulated to validate the ability of the LES to reproduce the mean and fluctuating velocity fields measured in the experiments of Agarwal et al. (2018). Such comparison provides confidence that the pressure field, which is central to inception, is accurately represented by our methodology of prescribing a turbulent boundary-layer at the inflow combined with LES. Agarwal et al. (2018) study this case for cavitation numbers in the range of $0.45 \leq \sigma \leq 0.55$, however as previously mentioned, no cavitation is observed within this range. Once the velocity field is validated, we evaluate the cavitation model by dropping the inflow pressure to yield $\sigma = 0.25$. It is important to mention that this is not the inception σ. The process of finding the inception σ requires lowering the inflow pressure slowly and checking if there are instants of time where the local pressure is lower than vapor pressure. Different from the validation case in Section 3.1, this task becomes demanding and computationally expensive for high Re. Given the amounts of vapor produced relative to the freestream levels, displayed later in this section, $\sigma = 0.25$ would be a case between inception and developed cavitation.

The inflow turbulent boundary-layer is generated on a separate flat plate domain with a grid resolution of $\Delta x^+ = 37$, $\Delta y^+ = 0.38$ and $\Delta z^+ = 20$. Fig. 4 shows the boundary-layer colored by axial velocity and its validation against the data of Schlatter and Örlü (2010). Good agreement is obtained for all quantities. Approximately 127 million cells are used in the backstep domain with $\Delta y^+ = 0.38$ and $\Delta x^+ = 20$ in the vicinity of the corner. The grid size is uniform in spanwise direction with $\Delta z^+ = 20$. A vapor concentration equivalent to $\alpha = 1\times10^{-5}$ is prescribed at the inflow. The velocity profiles are compared to experimental results of Agarwal et al. (2018) at $x = 1S$ and $x = 3S$ downstream of the step in Figs. 5 and 6, showing good agreement. The predicted reattachment length is around $L_r = 6.4S$, which compares reasonably well with the experimental value of $L_r = 6.2S$. Fig. 7 shows mean and fluctuation values of vapor volume fraction. Although cavitation is not observed experimentally at $Re_\tau = 800$, the work of Agarwal et al. (2018) reports that at different higher Re_τ and at different values of σ, the location where cavitation is observed is at $0.45 < x/L_r < 0.75$. It is evident from Fig. 7 that cavitation activity seems restricted to the region of $0.4 < x/L_r < 0.8$, consistent with experiments. The values of α along the shear layer are not provided by the experiments, thus we cannot compare them. However, this test shows that the model is able to simulate cavitation inception in complex flows.

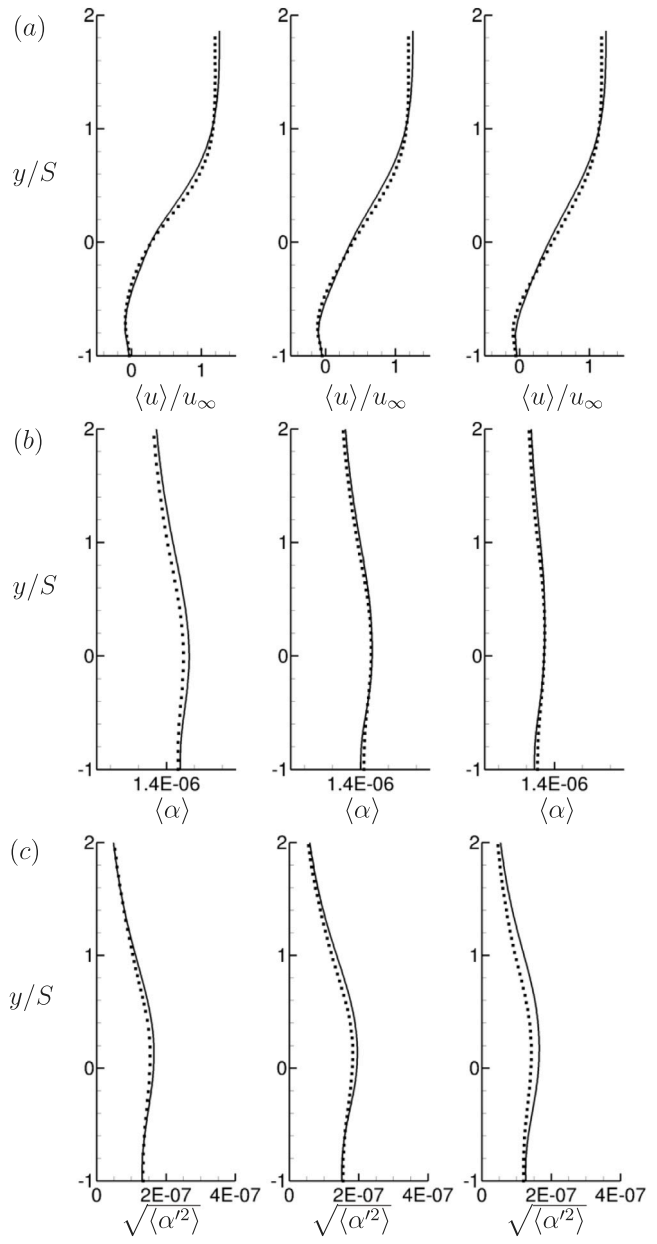

Fig. 3. Results from present model (lines) validated against model of Bhatt and Mahesh (2021) (symbols). Profiles from left to right are taken at $x = 1S$, $x = 2S$ and $x = 3S$ downstream of the step, respectively.

3.3. Flow over backstep at $Re_\tau = 1500$

Inception in the shear layer of the backstep is studied at $Re_\tau = 1500$ at the experimental conditions of $\sigma = 0.55$ and $\sigma = 0.45$. The inflow turbulent boundary-layer is generated similarly to the previous case. The grid for this boundary-layer simulation has a resolution of $\Delta x^+ = 30$, $\Delta y^+ = 0.6$ and $\Delta z^+ = 32$. The flow field at an instant of time is illustrated in Fig. 8(a) showing the axially developing boundary-layer. Figs. 8(b) and (c) show validation against the data of Eitel-Amor et al. (2014). It can be seen that we obtain a good agreement in the inner layer, but underpredict the u_τ as well as the Reynolds stresses, which can be explained by the mesh resolution.

For the backward-facing step domain, the grid contains 190 million cells with $\Delta y^+ = 0.6$ and $\Delta x^+ = 12$ in the vicinity of the corner and a uniform $\Delta z^+ = 32$ in the spanwise direction. Similar to the previous case, a vapor concentration equivalent to $\alpha = 1 \times 10^{-5}$ is prescribed at the inflow. The flow field at the center plane, $x = 1S$ and $x = 3S$ are displayed in Fig. 9. Figs. 10 and 11 show a comparison between numerical and the experimental velocity profiles of Agarwal et al. (2018) at $x = 1S$ and $x = 3S$, respectively. Good agreement is obtained for the shear layer profiles despite the differences observed in the incoming boundary-layer, which can be explained by the use of a finer Δx^+ at the backstep inlet section ($x/S < 0$ in Fig. 9(a)). The reattachment length obtained is $L_r = 6.0S$, which is 9% larger than the experimental value of $L_r = 5.5S$.

3.3.1. Pressure and volume fraction statistics

Figs. 12(a) and (b) show probability density function (PDF) of pressure and volume fraction, respectively, between $x = 3S$ and $x = 6S$ for $\sigma = 0.55$. This region corresponds to the locations between $x = 0.5L_r$ and $x = L_r$. The measured pressure PDFs show a Gaussian behavior, which is also observed in Lee and Sung (2001). It can be noted that the probability of a low-pressure event is higher around half the reattachment point. According to the void fraction PDFs, the probability of finding regions of vapor seems confined around $x = 4S$, which is within the experimental range of Agarwal et al. (2018). Note that the location with a higher probability of a low-pressure event does not necessarily match the location with a high probability of finding vapor at inception conditions. The stations at $x = 3S$ and $x = 4S$, for instance, have PDF curves for pressure showing similar probability for vapor pressure but their probabilities for volume fraction are orders of magnitude apart. This indicates the effects of finite rate evaporation and condensation. Regions at vapor pressure need to be sustained for a finite amount of time to allow for the growth of vapor to more visible sizes. Fig. 12(a) and (b) show that, for $\sigma = 0.55$, the cavitation process starts at $x = 3S$ and the vapor grows slowly as it is advected following the low-pressure regions to $x = 4S$. Over this distance of one step height, the PDF of void fraction reveals that vapor, most likely, only grows by 0.05%. This very small increase may imply that these incipient structures that start forming at $x = 3S$ do not remain at vapor pressure for their entire travel to $x = 4S$. As the vapor is advected further to $x = 5S$, it is condensed back to freestream levels due to a pressure recovery as shown by the PDFs. Additionally, Fig. 12(a) exposes how violent the pressure fluctuations can be in such flows. Observe how the most likely value for pressure obtained between $x = 3S$ and $x = 4S$ lies around 25 kPa. The tails of the curves, however, suggest that pressure can go as low as vapor pressure. These drastic fluctuations were also noticed in O'Hern (1990) and help to clarify why inception can be seen in a shear flow at a relatively high ambient pressure.

The PDFs of pressure and volume fraction are also computed for $\sigma = 0.45$ and are displayed in Fig. 13. For all locations, the curves in Fig. 13(a) show a peak probability at a lower value of pressure than those obtained for $\sigma = 0.55$ in Fig. 12(a), as expected. It can also be observed that there is a higher probability of finding larger volumes of vapor, which is also foreseen. Note that all stations exhibit some probability of having regions at vapor pressure or lower, in contrast to $\sigma = 0.55$. Similar to $\sigma = 0.55$, the magnitude of the most likely observed pressure increases with axial distance from the step. However, in contrast to $\sigma = 0.55$, the location with a higher likelihood of finding vapor matches the location most likely to experience very low pressure. Note how the tail of the pressure PDF curves show that violent pressure fluctuations are seen at $x = 5S$. These extremely low values of pressure increase the evaporation rates, which are responsible for the explosive growth obtained at the same location.

The inception event rates at $\sigma = 0.55$ and $\sigma = 0.45$ are computed and displayed in Figs. 14(a) and (b) respectively. These events are obtained by counting the number of events with $p \leq p_v$ across the shear layer over two entire flow-throughs and averaging them over the span direction. The decrease in cavitation number from 0.55 to 0.45 is found to increase the inception activity by around $O(1)$. It can be observed that most of the captured structures are located between

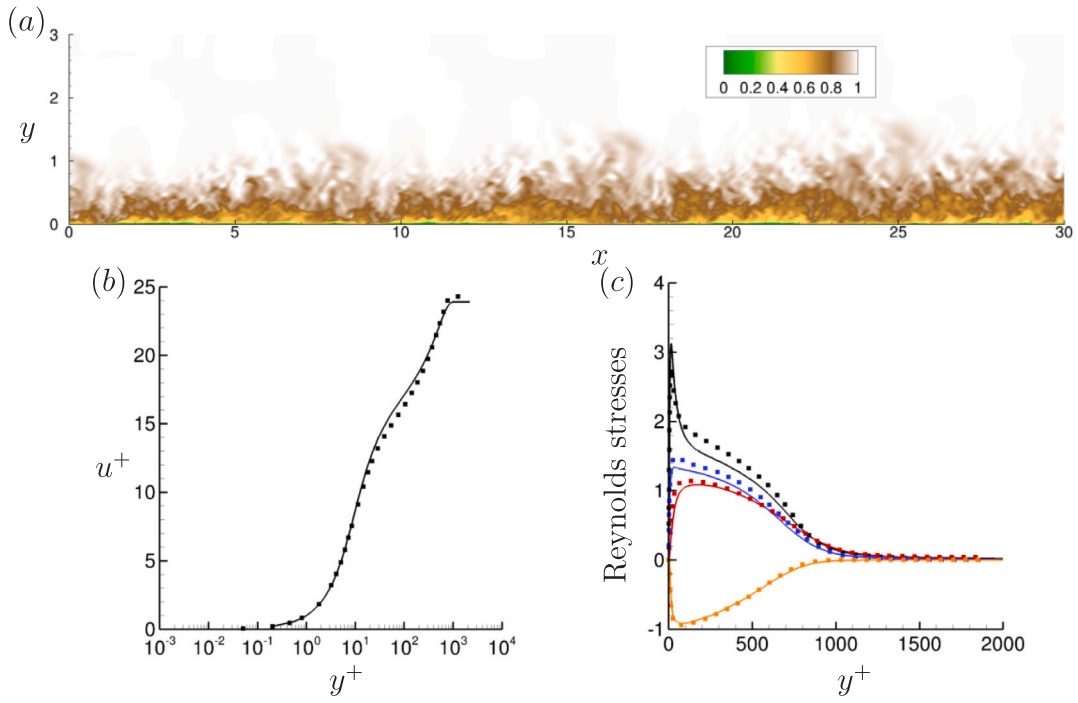

Fig. 4. Turbulent boundary-layer colored by axial velocity (a). Mean values of axial velocity (b) and values of Reynolds stresses (c) at $Re_\tau = 800$. Simulation results (lines) compared against data from Schlatter and Örlü (2010) (symbols). Black, red, blue and orange lines and symbols in (c) represent, respectively, $\sqrt{\langle u'^2\rangle}/u_\infty$, $\sqrt{\langle v'^2\rangle}/u_\infty$, $\sqrt{\langle w'^2\rangle}/u_\infty$ and $\langle u'v'\rangle/u_\infty^2$. (For interpretation of the references to color in this figure legend, the reader is referred to the web version of this article.)

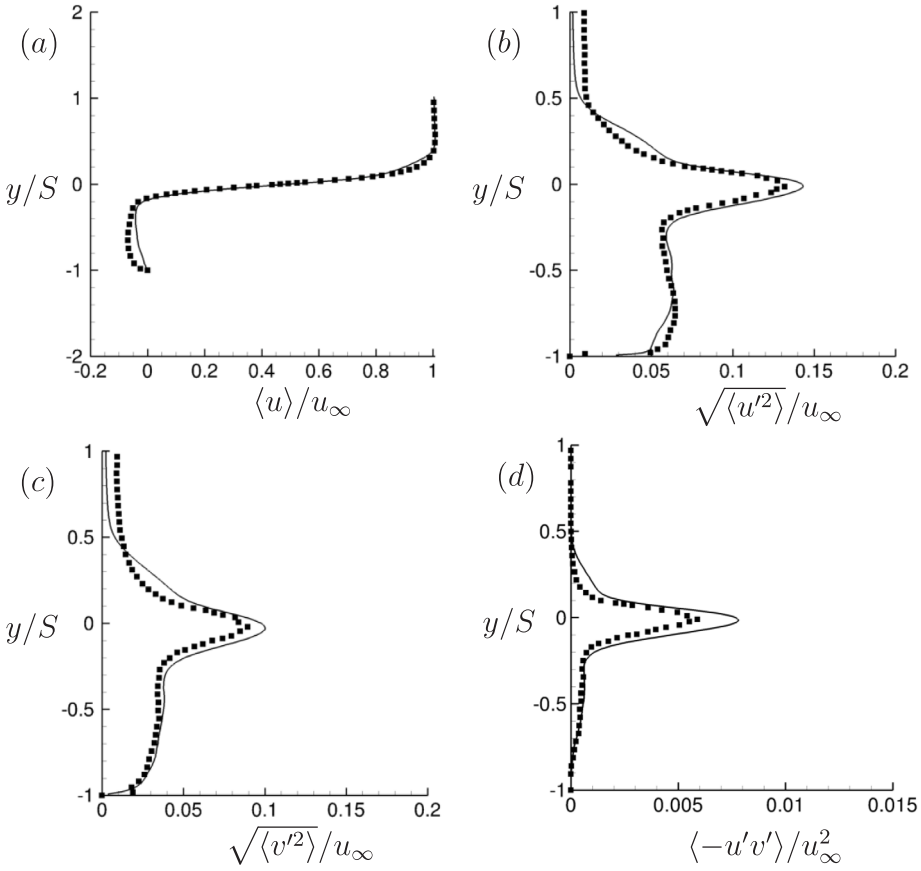

Fig. 5. Comparison between numerical (lines) and experimental (symbols) profiles of mean velocity and Reynolds stresses for $Re_\tau = 800$ at $x = 1S$ downstream of the step. S represents the step height. The experimental values are obtained from the work of Agarwal et al. (2018).

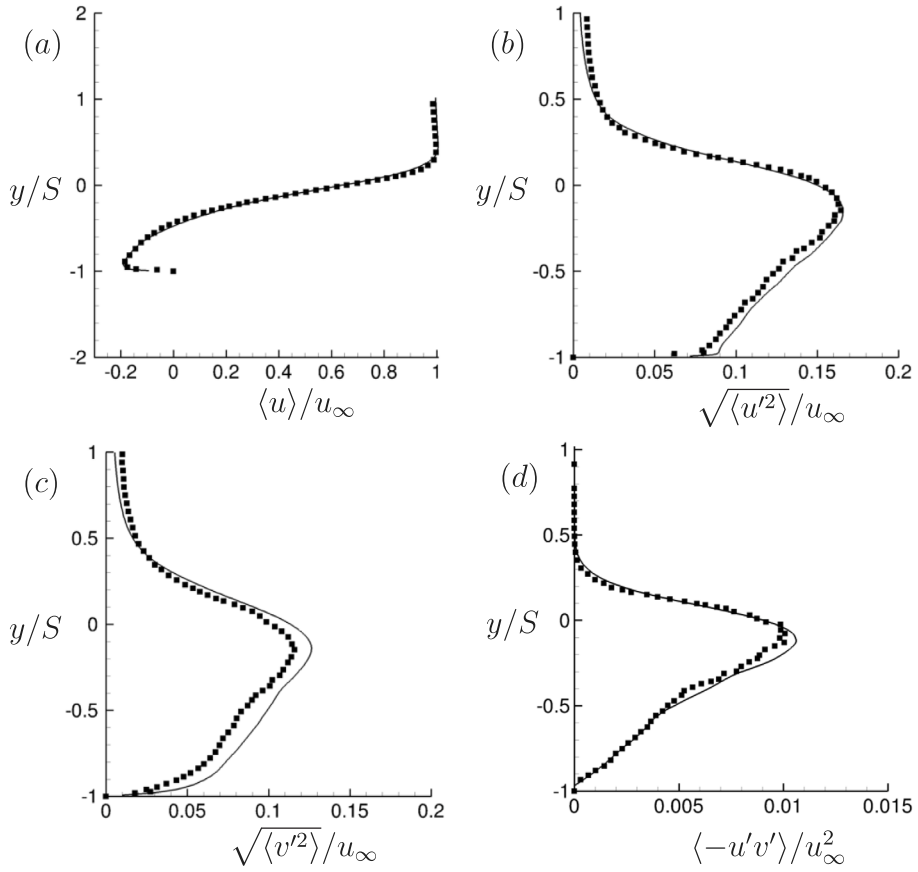

Fig. 6. Comparison between numerical (lines) and experimental (symbols) profiles of mean velocity and Reynolds stresses for $Re_\tau = 800$ at $x = 3S$ downstream of the step. S represents the step height. The experimental values are obtained from the work of Agarwal et al. (2018).

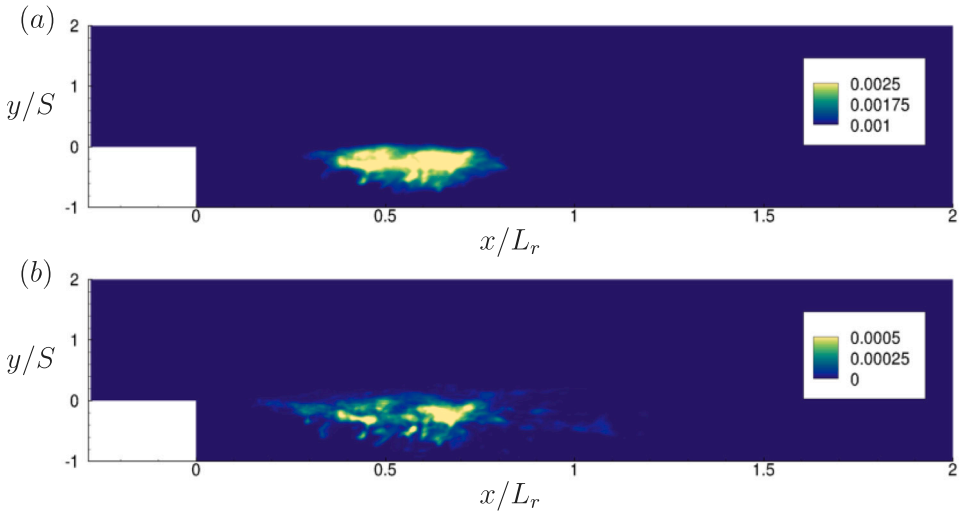

Fig. 7. Contours of $\langle \alpha \rangle$ and $\langle \alpha'^2 \rangle$ are given in (*a*) and (*b*), respectively, for $\sigma = 0.25$ at $Re_\tau = 800$.

$0.4 < x/L_r < 0.8$, consistent with the experimental data of Agarwal et al. (2018). For $\sigma = 0.45$, however, some structures are also detected at a considerable frequency downstream of the experimental range, compatible with the PDF curves of Fig. 13. Furthermore, it can be noted that although these incipient structures are scattered throughout the shear layer for $\sigma = 0.55$, they cover small continuous regions in an axial direction indicating that they only cavitate for very brief periods.

Although Figs. 12 and 13 show the likelihood of low pressure in some regions, they do not indicate the most probable cavitating pressure. This information is provided in Fig. 15 for both cases. These

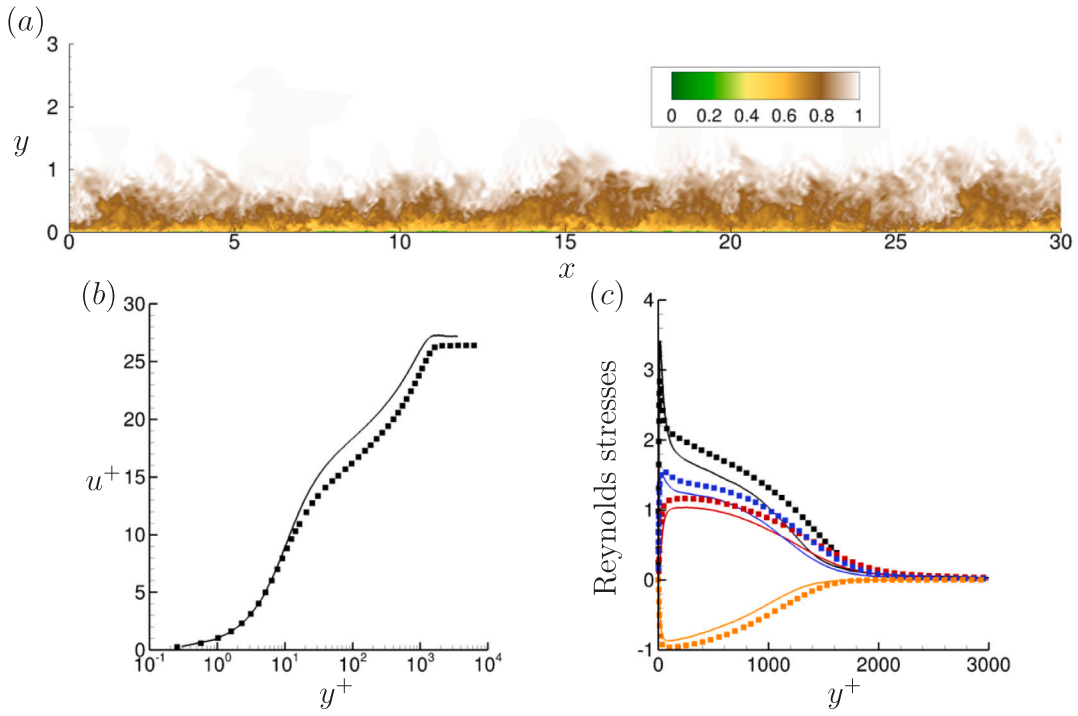

Fig. 8. Turbulent boundary-layer colored by u/u_∞ (*a*). Mean values of axial velocity (*b*) and values of Reynolds stresses (*c*) at $Re_\tau = 1500$. Simulation results (lines) compared against data from Eitel-Amor et al. (2014) (symbols). Black, red, blue and orange lines and symbols in (*c*) represent, respectively, $\sqrt{\langle u'^2\rangle}/u_\infty$, $\sqrt{\langle v'^2\rangle}/u_\infty$, $\sqrt{\langle w'^2\rangle}/u_\infty$ and $\langle u'v'\rangle/u_\infty^2$. (For interpretation of the references to color in this figure legend, the reader is referred to the web version of this article.)

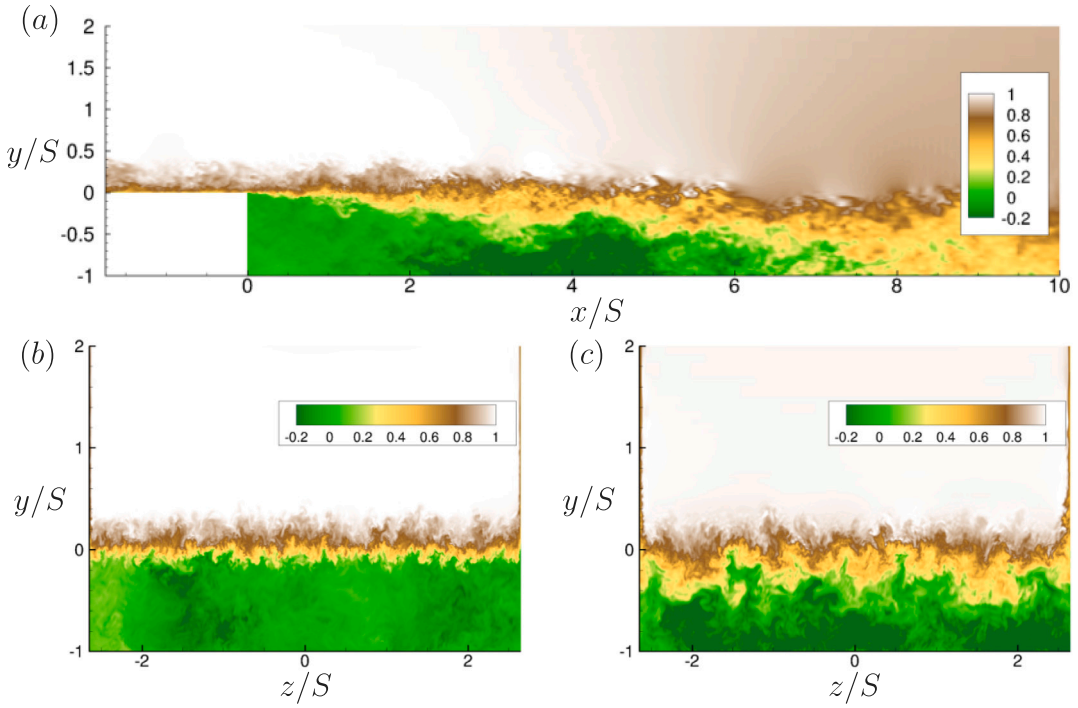

Fig. 9. Instantaneous flow field colored with u/u_∞ for $Re_\tau = 1500$ at center plane (*a*) and at positions $x = 1S$ (*b*) and $x = 3S$ (*c*) downstream of the step. S represents the step height. (For interpretation of the references to color in this figure legend, the reader is referred to the web version of this article.)

curves indicate that the most plausible cavitating pressure is around −1500 Pa for $\sigma = 0.55$ and −5500 Pa for $\sigma = 0.45$. Since both cases are performed for the same Re_τ, the drop in the inflow cavitation number was obtained by dropping inflow pressure by 17%. This small drop in inflow pressure changes the magnitude of the most likely cavitating pressure by around 3.5 times. As it will be demonstrated in the next section, these pressure minima are found to be located inside the cores of the stretched streamwise vortices.

3.3.2. Flow topology of incipient structures

O'Hern (1990) found that inception would primarily occur in the elongated quasi-streamwise vortices (QSV), indicating that the lowest

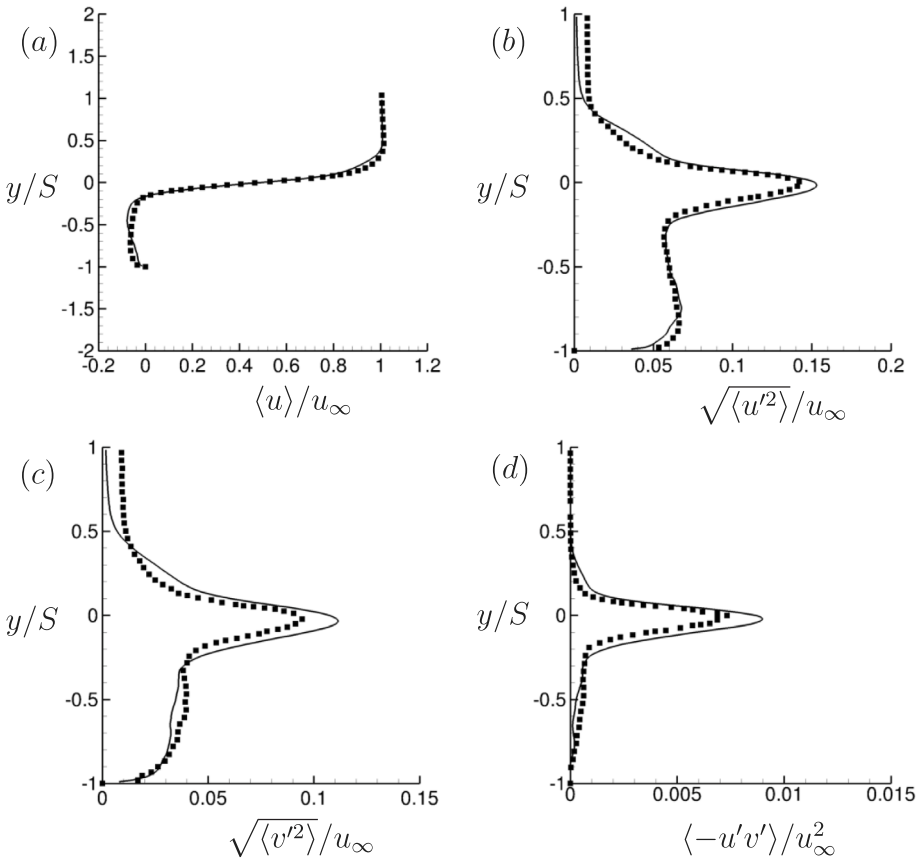

Fig. 10. Comparison between numerical (lines) and experimental (symbols) profiles of mean velocity and Reynolds stresses for $Re_\tau = 1500$ at $x = 1S$ downstream of the step. S represents the step height. The experimental values are obtained from the work of Agarwal et al. (2018).

values of pressure are expected to be in the core of these vortices. In this work, we examine the incipient structures by studying their flow topology based on the invariants of the velocity gradient tensor, strain rate tensor and rotation rate tensor. Chong et al. (1990), Cantwell (1992) and Perry and Chong (1994) discuss the details of this approach; only a summary of the invariants and their physical meaning will be given here. The velocity gradient tensor, $A_{ij} = \frac{\partial u_i}{\partial x_j}$, has the following characteristic equation:

$$\lambda_i^3 + P\lambda_i^2 + Q\lambda_i + R = 0, \tag{10}$$

where λ_i are the eigenvalues and P, Q and R are the first, second and third invariants of A_{ij}, respectively. These invariants are given by

$$\begin{aligned} P &= -S_{ii}, \\ Q &= \frac{1}{2}(P^2 - S_{ij}S_{ji} - \Omega_{ij}\Omega_{ji}), \\ R &= \frac{1}{3}(-P^3 + 3PQ - S_{ij}S_{jk}S_{ki} - 3\Omega_{ij}\Omega_{jk}S_{ki}). \end{aligned} \tag{11}$$

Here, $S_{ij} = \frac{A_{ij}+A_{ji}}{2}$ and $\Omega_{ij} = \frac{A_{ij}-A_{ji}}{2}$ are the strain rate tensor and rotation rate tensor, respectively. $P = 0$ due to incompressibility. Likewise, the invariants of S_{ij} and Ω_{ij} are defined by their respective characteristic equation. For incompressible flows, only the second and third invariants of S_{ij} and the second invariant of Ω_{ij} are non-zero. They are given by the following expressions:

$$Q_s = -\frac{1}{2}S_{ij}S_{ji}, \quad R_s = -\frac{1}{3}S_{ij}S_{jk}S_{ki} \quad \text{and} \quad Q_w = -\frac{1}{2}\Omega_{ij}\Omega_{ji}, \tag{12}$$

where the subscripts S and w indicate that the variable is related to the strain rate tensor and rotation rate tensor, respectively.

Fig. 16(a) shows the topologies in the Q–R plane. The tent-like curve depicts $D = 0$, where D is the discriminant of A_{ij} given by $D = \frac{27}{4}R^2 + Q^3$. Fluid elements occupying the region of $D > 0$ are focal regions and can be undergoing stretching ($R < 0$) or contraction ($R > 0$). According to Ooi et al. (1999), the focal structures with stretching topology are in general elongated and compact in a tube-like shape, while the contracting regions resemble 'blobs' and are usually found at the ends of the focal structure or at the intersection between two stretching regions. Fig. 16(b) shows the physical interpretation for the Q_s–Q_w plane. Regions of the flow lying below the $Q_w = -Q_s$ line are dominated by rotation (such as the core of a vortex tube) while regions lying above the line are dominated by strain (such as the periphery of a vortex tube) with intense kinetic energy dissipation. The third invariant of the strain rate tensor (R_s) is proportional to the strain skewness and it can be demonstrated that $R_s = -\lambda_1\lambda_2\lambda_3$ (da Silva and Pereira, 2008), where $\lambda_1 > \lambda_2 > \lambda_3$ are the eigenvalues of S_{ij} and $\lambda_1 + \lambda_2 + \lambda_3 = 0$ due to incompressibility. Thus, the Q_s–R_s plane is useful to investigate the geometry of the local straining of a fluid particle. Curves representing the ratio between the principal strain rates $\lambda_1 : \lambda_2 : \lambda_3$ are shown in Fig. 16(c), where each of them indicates a flow geometry (e.g. $1 : 1 : -2$ indicates axisymmetric stretching while $2 : -1 : -1$ corresponds to axisymmetric contraction). For more details, the reader is referred to Perry and Chong (1994).

We collect the values of these invariants over time for the regions where the local pressure is lower than vapor pressure and compute their joint-PDFs in the Q–R, Q_s–Q_w and Q_s–R_s planes. The joint-PDFs, however, do not indicate whether these vortices are in the streamwise direction. The work of Agarwal et al. (2020) identifies the quasi-streamwise vortices by the threshold of $\sqrt{\omega_x^2 + \omega_y^2}/(u_\infty/S) > 3.5$, where ω_x and ω_y are the streamwise and vertical components of the vorticity, respectively. The PDF of this quantity is presented in Fig. 17(*a*) while Fig. 17(*b*) displays the probabilities for the angles between the vorticity vector and the velocity components, for the regions where the local pressure is lower than vapor pressure. It becomes evident that the obtained incipient structures are QSVs.

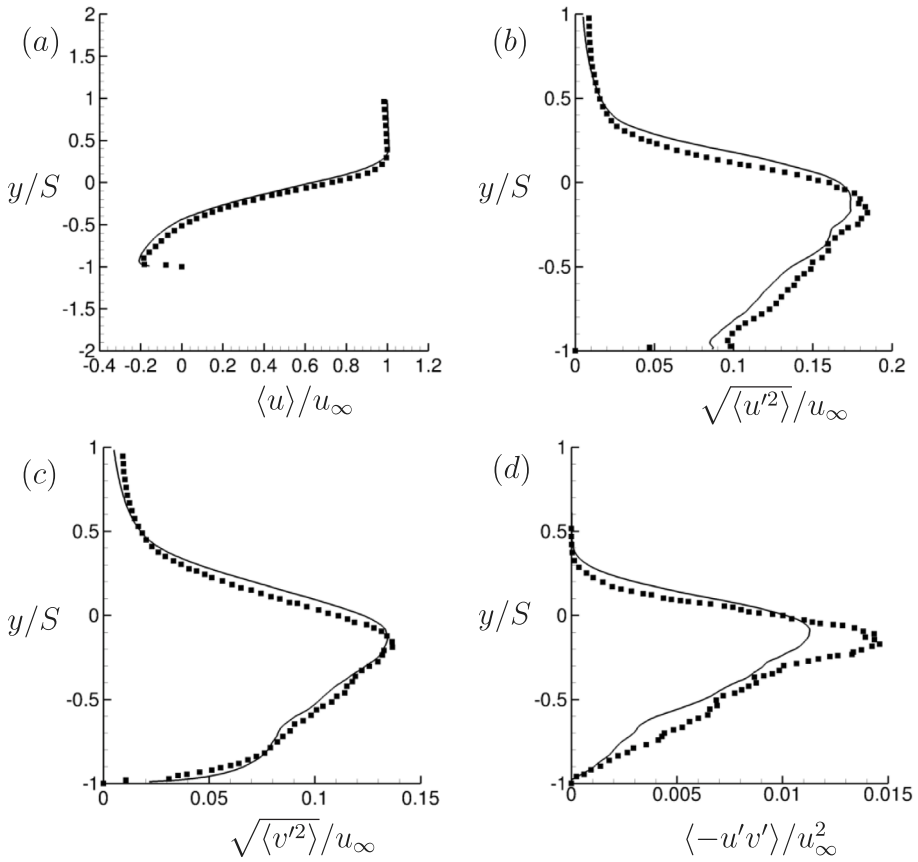

Fig. 11. Comparison between numerical (lines) and experimental (symbols) profiles of mean velocity and Reynolds stresses for $Re_\tau = 1500$ at $x = 3S$ downstream of the step. S represents the step height. The experimental values are obtained from the work of Agarwal et al. (2018).

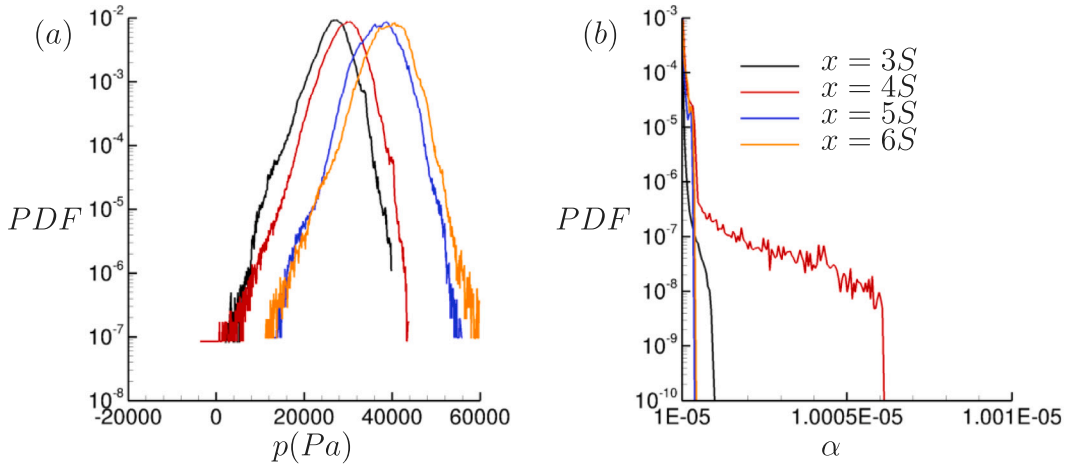

Fig. 12. Probability density function of pressure (a) and volume fraction (b) at different axial location for $\sigma = 0.55$. The y-axis in (b) is clipped at 10^{-10} for better visualization.

The joint-PDFs for the invariants for $\sigma = 0.55$ are shown in Fig. 18(a), (b) and (c) respectively. The results for $\sigma = 0.45$ are similar and are, therefore, not presented here. The joint-PDF of Q–R in Fig. 18(a) reveals that pressure drops below vapor pressure primarily in focal regions. The joint-PDF in Fig. 18(b) shows that these events are likely to be dominated by rotation. This reinforces the suggestion of O'Hern (1990). According to Fig. 18(c), these focal incipient structures show a tendency to have strain rate ratios of 2 : 1 : −3 or 3 : 1 : −4. In other words, this means that inception likely occurs in focal structures that are being elongated 2 or 3× more in their most extensive principal direction than in their intermediate principal direction. Fig. 19 shows a visual example of these structures. Isocontour of $p = p_v$ is given in orange and isocontour of $\alpha = 1.005\times10^{-5}$ is given in blue. The presence of multiple locations with a pressure equal to or less than vapor pressure in the shear layer can be observed, however, the largest structure is stretched in the streamwise direction. The isocontour of vapor volume fraction confirms that this structure cavitates first, which agrees with experimental observations.

Fig. 18(b) showed that regions of higher rotation rates are preferential sites for inception. However, it does not quantify the balance between rotation and straining. The kinematical vorticity number is often employed as a quantitative measurement of the amount of rotation

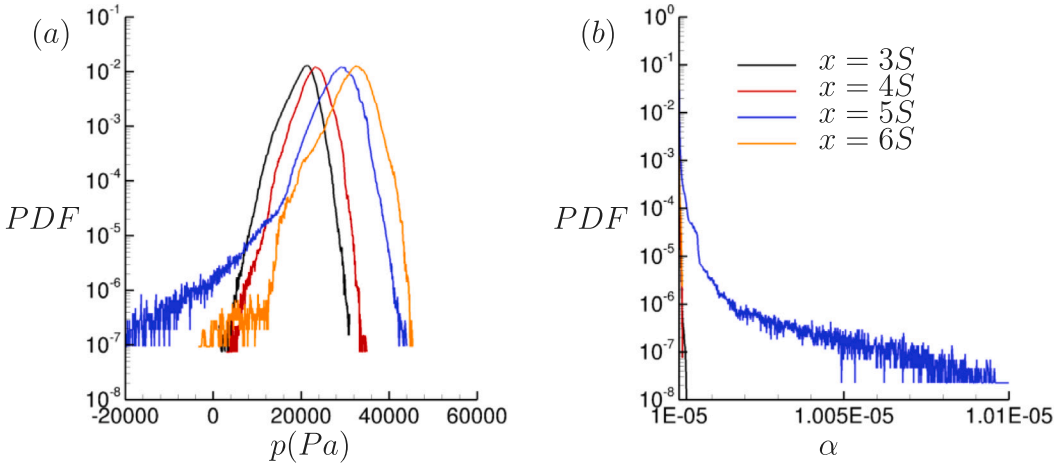

Fig. 13. Probability density function of pressure (*a*) and volume fraction (*b*) at different axial location for $\sigma = 0.45$. The y-axis in (*b*) is clipped at 10^{-8} for better visualization.

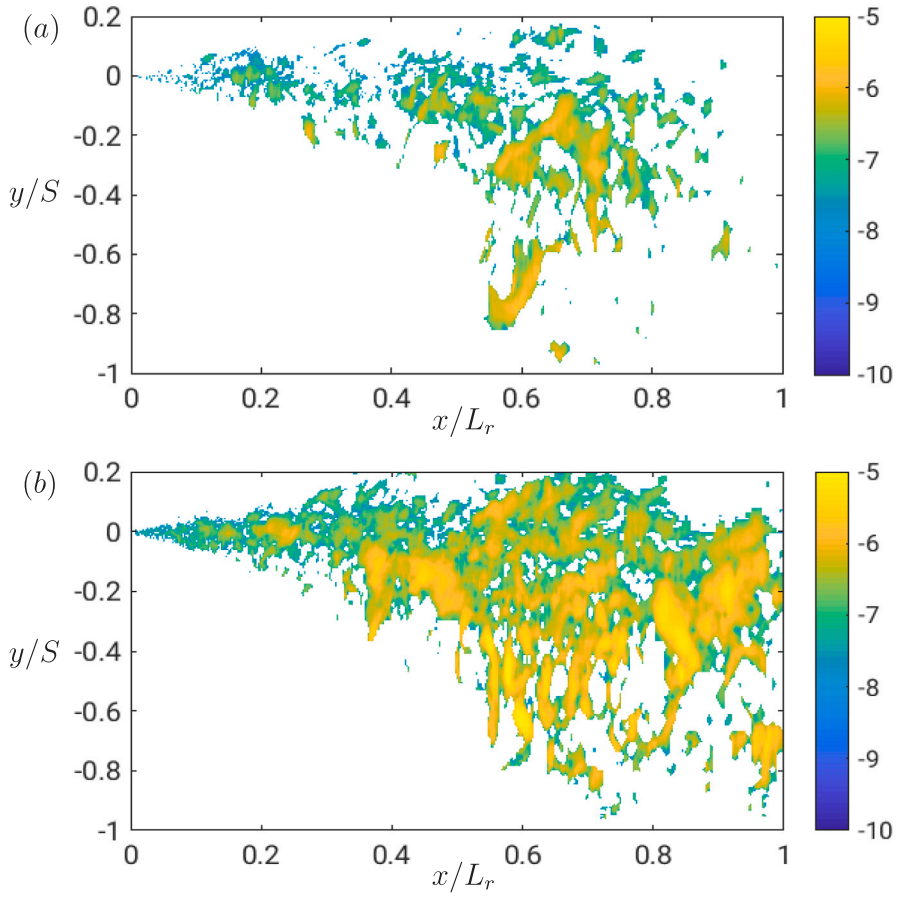

Fig. 14. Inception event rates for $\sigma = 0.55$ (*a*) and $\sigma = 0.45$ (*b*). Levels in both plots are in logarithmic scale.

of a fluid particle (Truesdell, 1954), and is defined as

$$\kappa = \left(\frac{Q_w}{-Q_s} \right)^{\frac{1}{2}}. \tag{13}$$

This variable measures the ratio between rotational strength and irrotational stretching (Ooi et al., 1999). A value of $\kappa = 0$ implies that a fluid particle is undergoing purely irrotational stretching while a value of $\kappa = \infty$ means that the fluid particle is subjected only to solid-body rotation. The joint-PDF between pressure and κ is displayed in Fig. 20 and reveals a predominance of $\kappa \approx 2$, which means that inception is most likely to occur in the cores of vortex tubes subjected to a rotation rate 4× stronger than the stretching rate. Additionally, a decreasing pressure and consequently the likelihood of cavitation is found to be correlated to an increasing κ.

4. Summary

A method is developed to simulate and predict cavitation inception. The method consists of treating vapor as a passive scalar in an incompressible liquid. An advection–diffusion equation with a source term is solved for the concentration of vapor in a dual time step procedure, allowing for higher time steps. Convective and diffusive

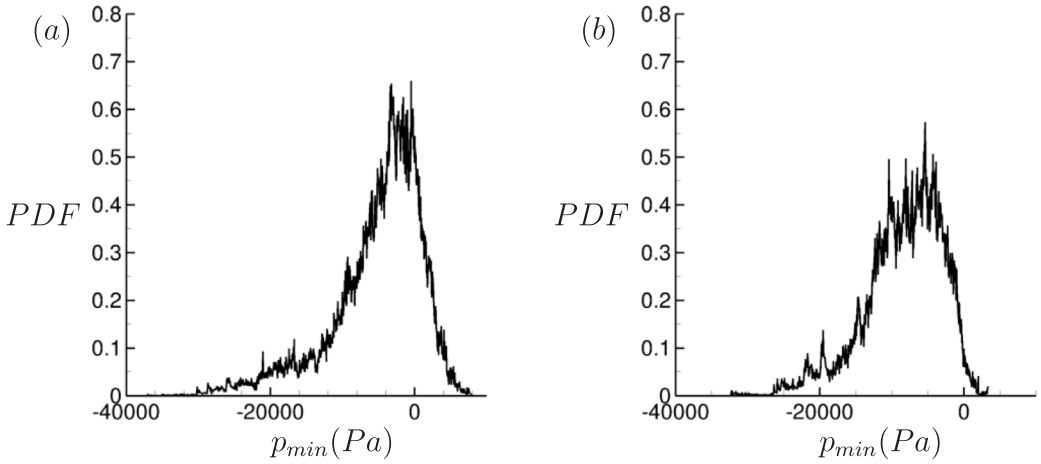

Fig. 15. Probability density function of minimum pressure for $\sigma = 0.55$ (*a*) and $\sigma = 0.45$ (*b*).

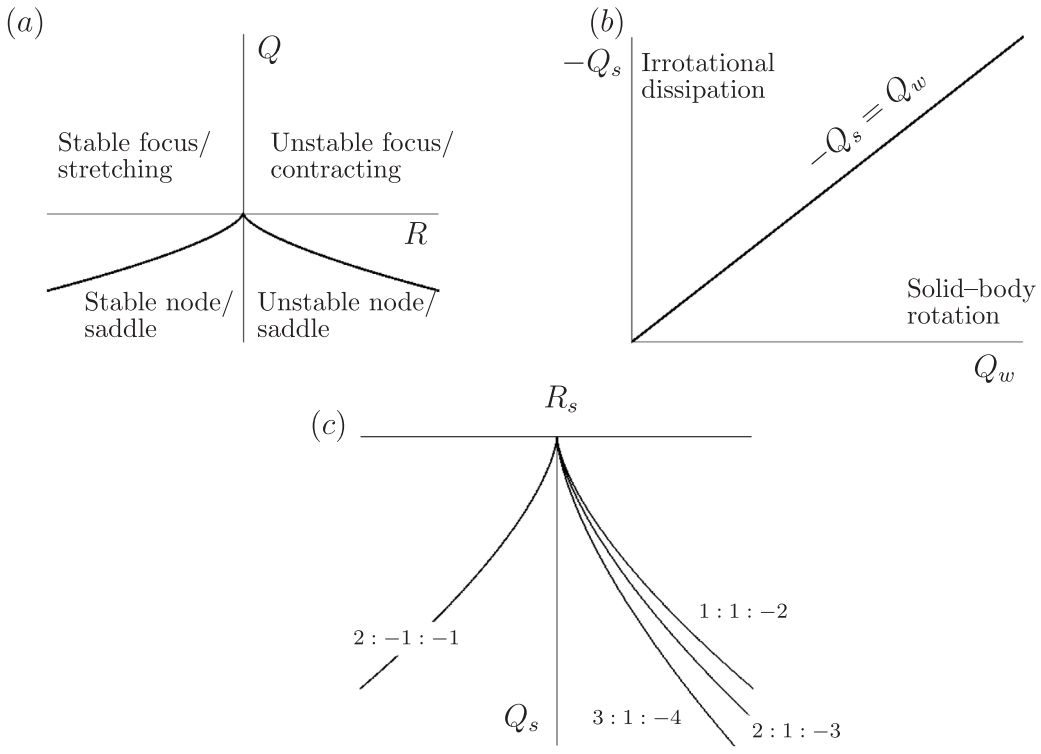

Fig. 16. The regions formed by the second and third invariants of the velocity gradient tensor (Q–R) and the regions formed by the second invariants of the strain rate tensor and rotation rate tensor (Q_s–Q_w) are given in (*a*) and (*b*) respectively with their corresponding flow patterns. Curves representing the ratio between the principal strain rates are shown in the Q_s–R_s plane in (*c*).

fluxes are obtained with an approach based on a least-square method that provides accurate results on skewed meshes. The source term is split into terms that are treated explicitly and implicitly, yielding a stable solution as shown in the Appendix. We validate the model against results obtained using the compressible homogeneous mixture approach. Inception in the shear layer of a backstep is investigated in the experimental configuration of Agarwal et al. (2018) with inflow turbulent boundary-layers at $Re_\tau = 800$ and 1500. The case of $Re_\tau = 800$ does not show cavitation for the range of σ studied in the experiments. Therefore, we simulate this case at a lower ambient pressure as a verification test. For $Re_\tau = 1500$, we study the experimental conditions of $\sigma = 0.55$ and $\sigma = 0.45$. Pressure and void fraction statistics are computed and the likelihood of cavitation exhibits good agreement with experimental data. The inception event rates show an increase by around $O(1)$ when the cavitation number is reduced from $\sigma = 0.55$ to $\sigma = 0.45$ and are more likely to occur around $0.4 < x/L_r < 0.8$. The flow topology is investigated and the cores of the stretched quasi-streamwise vortices (QSV) are found to be the preferred sites for inception. Additionally, the ratio between rotation and strain rates and its relation with inception was investigated. It was observed that inception most likely occurs when the rotation rate of the vortex tube is 4× stronger than the stretching rate. The pressure inside the QSVs are found to be −1500 Pa and −5500 Pa for $\sigma = 0.55$ and $\sigma = 0.45$, respectively. Lastly, an analysis reveals a predominance for the ratio between the principal strain rates of $2 : 1 : -3$ and $3 : 1 : -4$ for the cavitating QSVs.

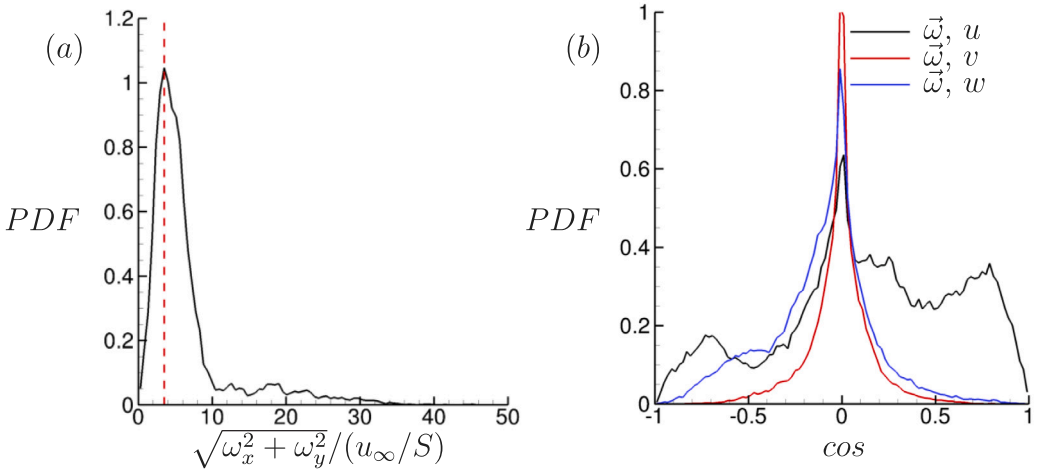

Fig. 17. PDFs of vorticity magnitude (a) and angle between vorticity vector and the velocity components (b). The red dashed line in (a) indicates $\sqrt{\omega_x^2+\omega_y^2}/(u_\infty/S) = 3.5$.

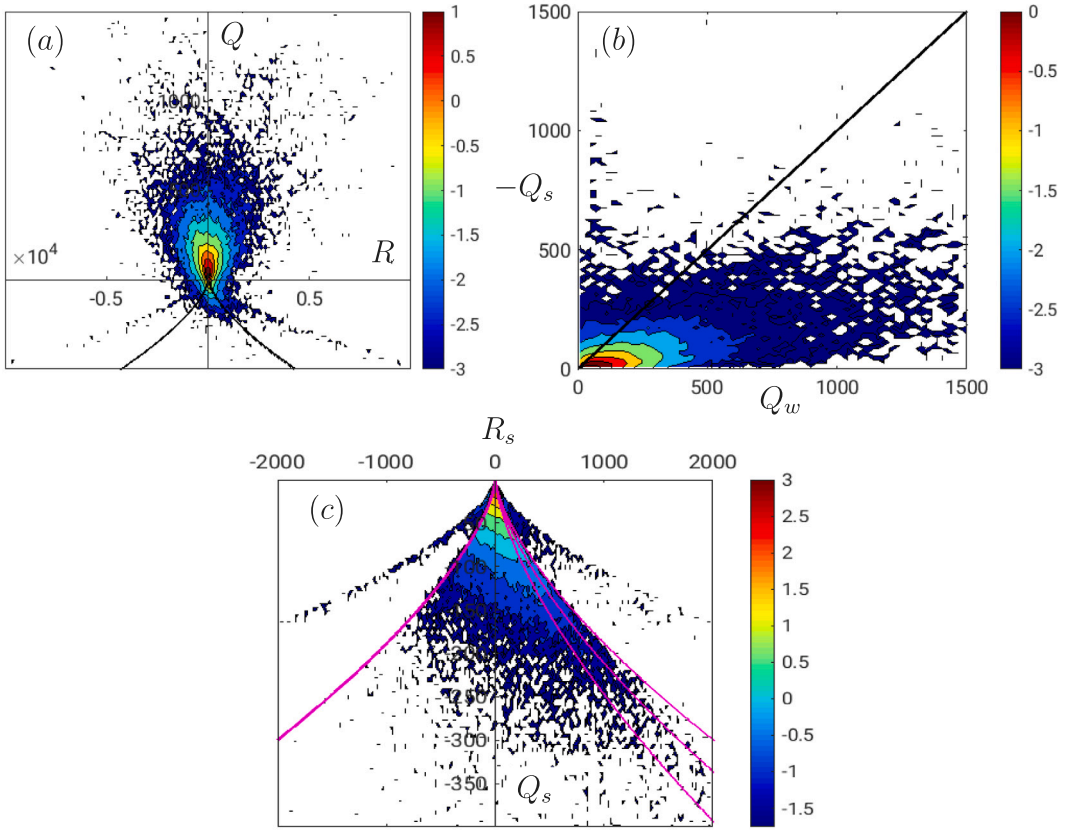

Fig. 18. Joint-PDFs of Q–R (a), Q_s–Q_w (b) and Q_s–R_s (c) plot for $\sigma = 0.55$. Levels in both plots are in logarithmic scale and the invariants are in non-dimensional units (using the appropriate combination of the step height, S, and the freestream velocity, u_∞).

CRediT authorship contribution statement

Filipe L. Brandao: Gridding, Code development, Problem investigation results postprocessing, Writing. **Krishnan Mahesh:** Problem investigation, Writing - review & editing.

Declaration of competing interest

The authors declare that they have no known competing financial interests or personal relationships that could have appeared to influence the work reported in this paper.

Acknowledgments

This work is supported by the United States Office of Naval Research under grant ONR N00014–17–1–2676 with Dr. Ki–Han Kim as the program manager. Computing resources were provided by the High-Performance Computing Modernization Program (HPCMP). We thank Ms. Karuna Agarwal and Professor Joseph Katz for providing the experimental data.

Appendix. Treatment of source terms

The source terms can have a big impact on the reliability of numerical solutions as they can drive them to unphysical values. In our

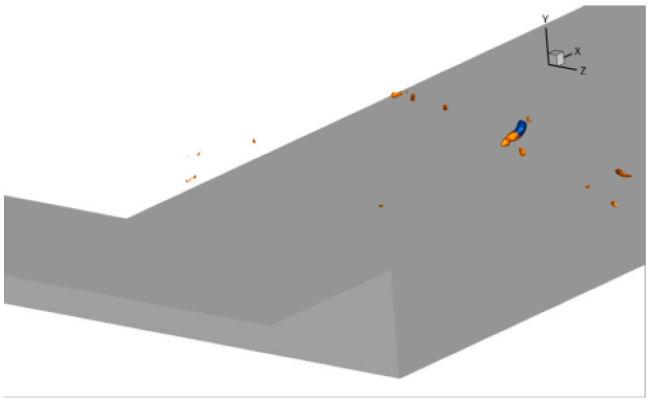

Fig. 19. Isocontours of $p = p_v$ in orange and $\alpha = 1.005\times10^{-5}$ in blue. (For interpretation of the references to color in this figure legend, the reader is referred to the web version of this article.)

case, these unrealistic solutions are $\alpha > 1$ and $\alpha < 0$. Usually, the source terms are better handled explicitly when they are positive, and implicitly when they are negative (sink) (Merci et al., 2000; Lian et al., 2010). For cavitation problems, we have both cases (see Eq. (3)). In the present work, they are treated as suggested in the work of Lian et al. (2010), where the source ($\bar{S}_e$) is divided between an equivalent sink and an enhanced source. We write the unfiltered version of the RHS of Eq. (3) in a generalized Crank–Nicolson form as

$$\begin{aligned} \ldots = &-\psi(\theta_1 S_e^{n+1} + (1-\theta_1)S_e^n) + (1+\psi)(\theta_2 S_e^{n+1} + (1-\theta_2)S_e^n) \\ &- (\theta_3 S_c^{n+1} + (1-\theta_3)S_c^n), \end{aligned} \tag{A.1}$$

where the parameters θ_1, θ_2 and θ_3 can take the values of 0, 0.5 or 1 indicating explicit, Crank–Nicolson or implicit formulation, respectively. The first, second and third terms in the RHS of Eq. (A.1) are the equivalent sink, the enhanced source and the original sink, respectively. Due to the non-linear nature of both source and sink terms, they are linearized following a Taylor series expansion with respect to the vapor concentration as

$$\begin{aligned} S_e^{n+1} &= S_e^n + \frac{\partial S_e}{\partial C}^n (C^{n+1} - C^n), \\ S_c^{n+1} &= S_c^n + \frac{\partial S_c}{\partial C}^n (C^{n+1} - C^n). \end{aligned} \tag{A.2}$$

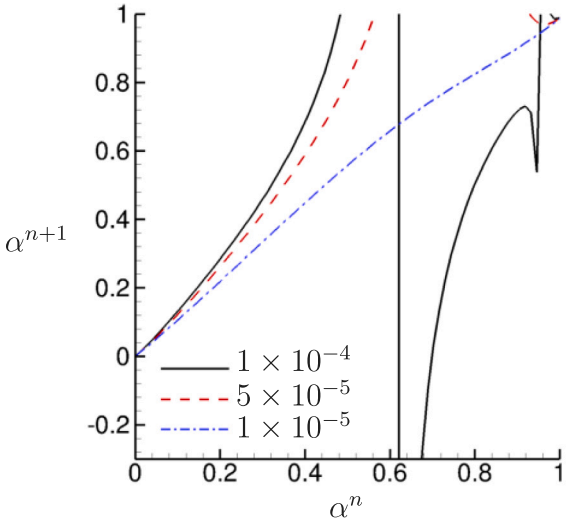

Fig. A.21. Change in solution for different scalar time steps.

Since $\alpha = C/\rho_v$, the partial derivatives of evaporation and condensation source terms are given by

$$\begin{aligned} \frac{\partial S_e}{\partial C} &= 2C(1 - 3\frac{C}{\rho_v} + 2\frac{C^2}{\rho_v^2})\frac{\rho_l}{\rho_v^3}C_e\frac{max(p_v - p, 0)}{\sqrt{2\pi R_v T}}, \\ \frac{\partial S_c}{\partial C} &= 2C(1 - 3\frac{C}{\rho_v} + 2\frac{C^2}{\rho_v^2})\frac{1}{\rho_v^2}C_c\frac{max(p - p_v, 0)}{\sqrt{2\pi R_v T}}. \end{aligned} \tag{A.3}$$

It was recommended in Lian et al. (2010) that both the original and equivalent sink should be treated implicitly ($\theta_1 = \theta_3 = 1$) while the enhanced source should be treated explicitly ($\theta_2 = 0$) with $\psi = 1$. This choice of parameters was shown to provide stable results when employed with a linear source term in Lian et al. (2010). However, the cavitation source and sink terms employed in this work are biquadratic. Although $\theta_3 = 1$ works well for the sink, we will show that the values for θ_1 and θ_2 need to be adjusted.

When $p < p_v$, only the source is activated and, ignoring the convective and diffusive fluxes, the change in vapor concentration during one time step (Δt_s) is given by

$$\Delta C = C^{n+1} - C^n = \frac{\Delta t_s S_e}{1 + \frac{\partial S_e}{\partial C}\Delta t_s(\psi\theta_1 - (1+\psi)\theta_2)}. \tag{A.4}$$

Fig. A.21 presents how the solution changes for different values of $\Delta t_s/t_r$ (where t_r is a given reference time), and for a given value of

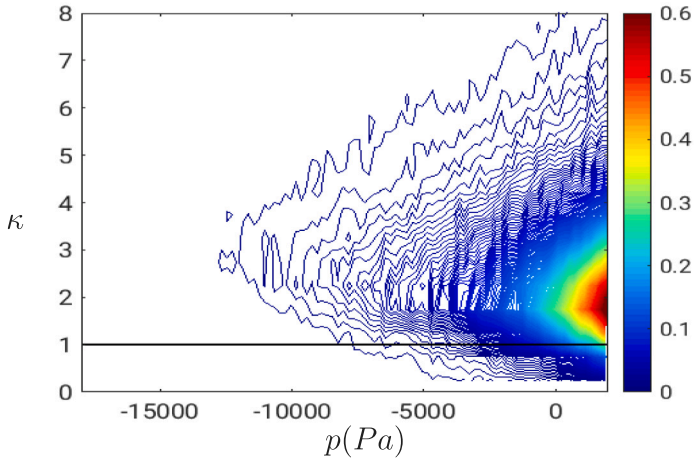

Fig. 20. Joint-PDF between pressure and κ for $\sigma = 0.55$. The line of $\kappa = 1$ signals the boundary between stretching to rotation dominated.

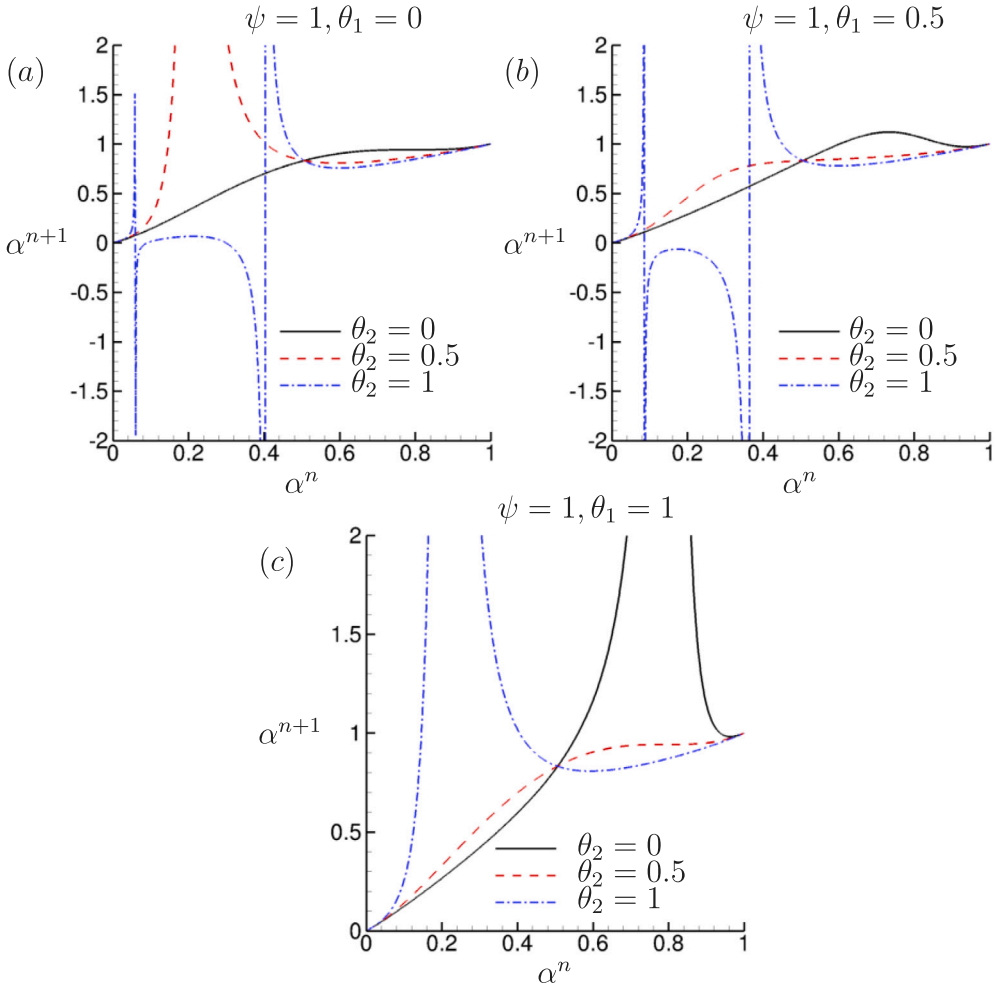

Fig. A.22. Change in solution for different choice of the parameters ψ, θ_1, θ_2 for $\Delta t_s/t_r = 5 \times 10^{-5}$.

pressure, when the parameters are chosen to be the same as suggested by Lian et al. (2010): $\psi = 1$, $\theta_1 = 1$ and $\theta_2 = 0$. Here, we have used a very large value for the empirical constant, $C_e = 200$ m^{-1}, to create a substantial growth of vapor concentration. Fig. A.21 reveals that, even when applying implicit time advancement for the transport equation, we need a time step as small as $\Delta t_s/t_r = 1 \times 10^{-5}$ for the vapor volume fraction to remain bounded in the {0, 1} range. Fig. A.22 shows the change in the void fraction at $\Delta t_s/t_r = 5 \times 10^{-5}$ for different combinations of the parameters ψ, θ_1 and θ_2. The first observation that can be made from Fig. A.22 is that the proper choice of parameters allow the solution to remain bounded even for higher time steps. It can be seen that when treating the enhanced source explicitly ($\theta_2 = 0$) as suggested in Lian et al. (2010), values of α within the range of {0, 1} are only achieved when the equivalent sink is also treated explicitly ($\theta_1 = 0$). We can see that three combinations of parameters provide limited cavitation: $\theta_1 = \theta_2 = 0$, $\theta_1 = \theta_2 = 0.5$ and $\theta_1 = 1$ with $\theta_2 = 0.5$.

A question remains of why these combinations work and why their α^{n+1} curves have different slopes. A logical way to study this would be through von Neumann stability analysis. However, due to the non-linear nature of the source term, this task becomes unnecessarily hard. Consequently, we follow the approach in Patankar (1980). Applying Eq. (A.2) into the RHS of Eq. (A.1), the linearized evaporation source term becomes

$$\begin{aligned} S_{el} &= S_{ec} + S_{ep} C^{n+1}, \\ S_{ec} &= S_e^n - (-\psi\theta_1 + (1+\psi)\theta_2)\frac{\partial S_e}{\partial C}^n C^n, \\ S_{ep} &= (-\psi\theta_1 + (1+\psi)\theta_2)\frac{\partial S_e}{\partial C}^n . \end{aligned} \tag{A.5}$$

Eq. (A.5) reveals that the different choices of parameters will result in distinctive slopes for S_{el}, which is plotted in Fig. A.23. The source term of Saito et al. (2007) has a region where $\frac{\partial S_e}{\partial C} > 0$ and another where $\frac{\partial S_e}{\partial C} < 0$ with the transition between them located at $\alpha = 0.5$. Therefore, in Fig. A.23 we show lines of S_{el} for values of C^n at these two different regions. A line with zero slope (horizontal) indicates that the solution is growing at a constant rate while lines with positive and negative slope mean an accelerated and decelerated solution change, respectively. The steeper the S_{el} line is, the faster the solution changes. If the time step is not small enough, combinations of the parameters that result in steeper S_{el} lines will lead to an unrealistic solution. This becomes clear when comparing Fig. A.23(a) with Fig. A.22(a) for $\psi = 1$ and $\theta_1 = 0$. Here we can see that increasing θ_2 from 0 to 1 makes the S_{el} line steeper and the only bounded solution occurs when $\theta_2 = 0$, which has zero slope. When $\theta_2 = 0.5$, the S_{el} line is a bit steeper than the S_e curve, leading to a solution of $\alpha^{n+1} > 1$ in Fig. A.22(a). When $\theta_2 = 1$, the S_{el} line becomes steeper and the solution blows-up even earlier. A combination of parameters that results in S_{el} lines with negative slopes are also preferable and recommended in Patankar (1980) since they imply a decelerated solution growth that allows for higher time steps. However, we can see in Fig. A.23 that no combination yields negative slopes in both regions of the S_e curve. Thus, we can see that the safer choices of parameters are $\theta_1 = \theta_2 = 0$, $\theta_1 = \theta_2 = 0.5$ and $\theta_1 = 1$ with $\theta_2 = 0.5$, which are the exact combinations that generated restricted solutions in Fig. A.22.

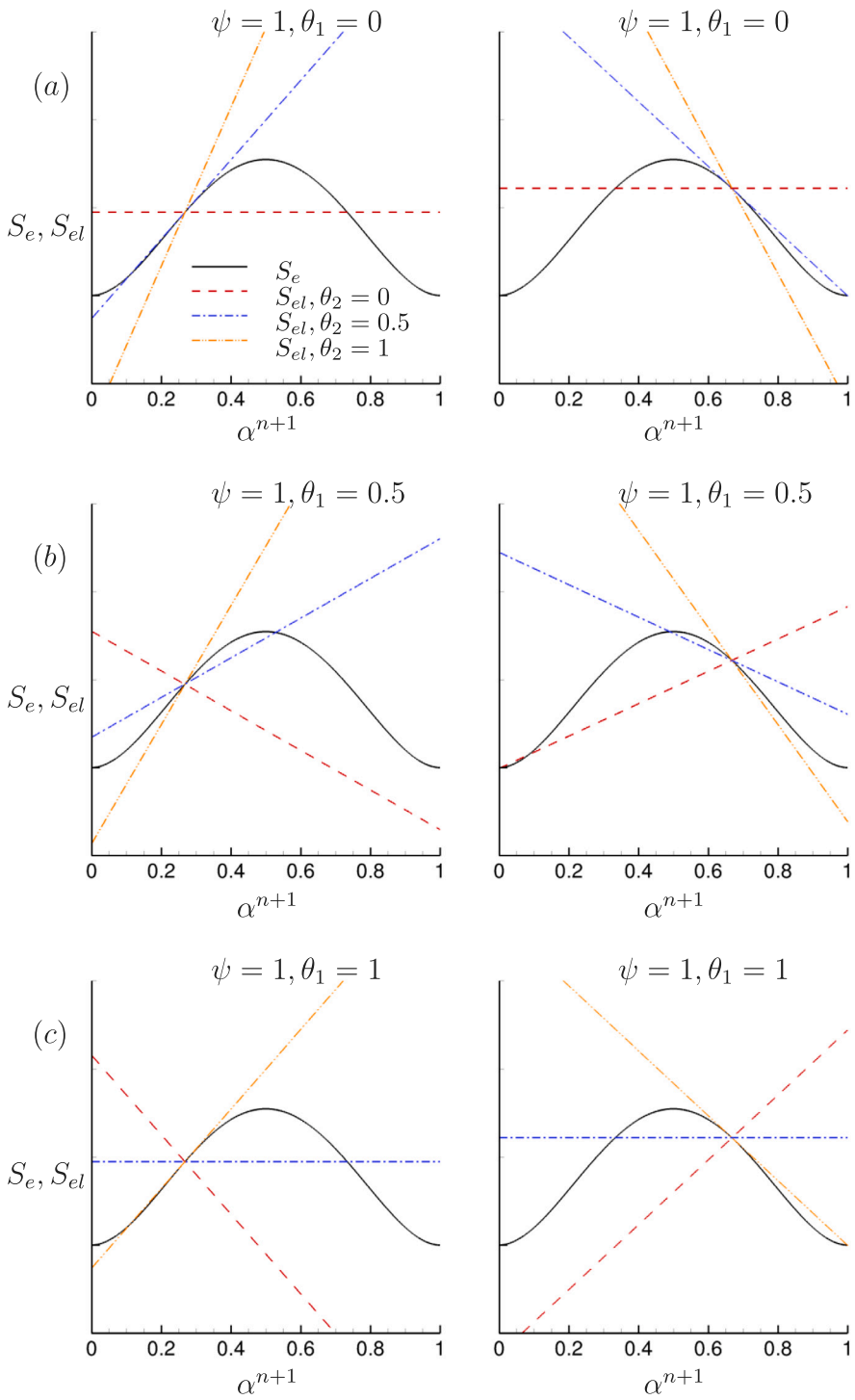

Fig. A.23. Comparison between the source term and its linearization. The plots on the left are for a specific C^n in the region where $\frac{\partial S_e}{\partial C} > 0$ and the plots on the right are for a specific C^n in the region where $\frac{\partial S_e}{\partial C} < 0$.

References

Aeschlimann, V., Barre, S., 2009. PIV-LIF determination of mean velocity field and reynolds stress tensor in a cavitating mixing layer. In: Proceedings of the 7th International Symposium on Cavitation. CAV2009.

Agarwal, K., Ram, O., Katz, J., 2018. Cavitating structures at inception in turbulent shear flow. In: Proceedings of the 10th International Symposium on Cavitation. CAV2018.

Agarwal, K., Ram, O., Wang, J., Lu, Y., Katz, J., 2020. Measuring the 3D pressure field and relating it to cavitation inception in a turbulent shear layer. In: Proceedings of the 33rd Symposium on Naval Hydrodynamics. Osaka, Japan.

Arndt, R.E.A., Arakeri, V.H., Higuchi, H., 1991. Some observations of tip–vortex cavitation. J. Fluid Mech. 229, 269–289.

Arndt, R.E.A., Keller, A.P., 1992. Water quality effects on cavitation inception in a trailing vortex. J. Fluids Eng. 114, 430–438.

Bappy, M., Martin, J.E., Li, J., Buscaglia, G.C., Carrica, P.M., 2019. A stochastic approach to cavitation inception prediction. In: Proceedings of the Sixth International Symposium on Marine Propulsors.

Bensow, R., 2011. Simulation of the unsteady cavitation on the the Delft Twist11 foil using RANS, DES and LES. In: Proceedings of the Second International Symposium on Marine Propulsors.

Bhatt, M., Mahesh, K., 2020. Numerical investigation of partial cavitation regimes over a wedge using large eddy simulation. Int. J. Multiph. Flow. 122, 103155.
Bhatt, M., Mahesh, K., 2021. A numerical approach to address the acoustic stiffness in cavitating flows. Int. J. Multiph. Flow. 141, 103568.
Brandao, F.L., Bhatt, M., Mahesh, K., 2020. Numerical study of cavitation regimes in flow over a circular cylinder. J. Fluid Mech. 885, A19.
Budich, B., Schmidt, S.J., Adams, N.A., 2018. Numerical simulation and analysis of condensation shocks in cavitating flow. J. Fluid Mech. 838, 759–813.
Cantwell, B.J., 1992. Exact solution of a restricted Euler equation for the velocity gradient tensor. Phys. Fluids A 4 (4), 782–793.
Chong, M.S., Perry, A.E., Cantwell, B.J., 1990. A general classification of three-dimensional flow fields. Phys. Fluids A 2 (5), 765–777.
da Silva, C., Pereira, C., 2008. Invariants of the velocity-gradient, rate–of–strain and rate–of–rotation tensors across the turbulent/nonturbulent interface in jets. Phys. Fluids 20 (5), 055101.
Egerer, C.P., Schmidt, S.J., Hickel, S., Adams, N.A., 2016. Efficient implicit LES method for the simulation of turbulent cavitating flows. J. Comput. Phys. 316, 453–469.
Eitel-Amor, G., Örlü, R., Schlatter, P., 2014. Simulation and validation of a spatially evolving turbulent boundary layer up to $Re_\theta = 8300$. Int. J. Heat Fluid Flow 47, 57–69.
Farrel, K.J., 2003. Eulerian/Lagrangian analysis for the prediction of cavitation inception. J. Fluids Eng. 125, 46–52.
Germano, M., Piomelli, U., Moin, P., Cabot, W.H., 1991. A dynamic subgrid-scale eddy viscosity model. Phys. Fluids A 3 (7), 1760–1765.
Gindroz, B., Billet, M.L., 1998. Influence of the nuclei on the cavitation inception for different types of cavitation on ship propellers. J. Fluids Eng. 120, 171–178.
Gnanaskandan, A., Mahesh, K., 2015. A numerical method to simulate turbulent cavitating flows. Int. J. Multiph. Flow. 70, 22–34.
Hsiao, C.T., Chahine, G.L., 2005. Scaling of tip vortex cavitation inception noise with a bubble dynamics model accounting for nuclei size distribution. J. Fluids Eng. 127 (1), 55–65.
Hsiao, C.T., Chahine, G.L., Liu, H.L., 2003. Scaling effect on prediction of cavitation inception in a line vortex flow. J. Fluids Eng. 125 (1), 53–60.
Iyer, C., Ceccio, S., 2002. The influence of developed cavitation on the flow of a turbulent shear layer. Phys. Fluids 14 (10), 3414–3431.
Katz, J., 1984. Cavitation phenomena within regions of flow separation. J. Fluid Mech. 140, 397–436.
Katz, J., O'Hern, T.J., 1986. Cavitation in large scale shear flows. J. Fluids Eng. 108, 373–376.
Khoo, M.T., Venning, J.A., Pearce, B.W., Brandner, P.A., 2020. Statistical aspects of tip vortex cavitation inception and desinence in a nuclei deplete flow. Exp. Fluids 61 (145).
Kumar, P., Mahesh, K., 2016. Towards large eddy simulation of hull–attached propeller in crashback. In: Proceedings of the 31st Symposium on Naval Hydrodynamics. California, USA.
Lee, I., Sung, H.J., 2001. Characteristics of wall pressure fluctuations in separated and reattaching flows over a backward–facing step. Exp. Fluids 30, 262–272.
Lian, C., Xia, G., Merkle, C.L., 2010. Impact of source terms on reliability of CFD algorithms. Comput. & Fluids 39, 1909–1922.
Lu, N.X., Svennberg, U., Bark, G., Bensow, R., 2012. Numerical simulations of the cavitating flow on a marine propeller. In: Proceedings of the 8th International Symposium on Cavitation. CAV2012.
Lund, T.S., Wu, X., Squires, K.D., 1998. Generation of turbulent inflow data for spatially-developing boundary layer simulations. J. Comput. Phys. 140 (2), 233–258.
Mahesh, K., Constantinescu, G., Moin, P., 2004. A numerical method for large-eddy simulation in complex geometries. J. Comput. Phys. 197 (1), 215–240.
Merci, B., Steelant, J., Vierendeels, J., Riemslagh, K., Dick, E., 2000. Computational treatment of source terms in two-equation turbulence models. AIAA J. 38 (11), 2085–2093.
Moin, P., Squires, K., Cabot, W., Lee, S., 1991. A dynamic subgrid-scale model for compressible turbulence and scalar transport. Phys. Fluids A 3 (11), 2746–2757.
Muppidi, S., Mahesh, K., 2008. Direct numerical simulation of passive scalar transport in transverse jets. J. Fluid Mech. 598, 335–360.
O'Hern, T.J., 1990. An experimental investigation of turbulent shear flow cavitation. J. Fluid Mech. 215, 365–391.
Ooi, A., Martin, J., Soria, J., Chong, M., 1999. A study of the evolution and characteristics of the invariants of the velocity–gradient tensor in isotropic turbulence. J. Fluid Mech. 381, 141–174.
Patankar, S.V., 1980. Numerical Heat Transfer and Fluid Flow, first ed. Taylor & Francis.
Perry, A.E., Chong, M.S., 1994. Topology of flow patterns in vortex motions and turbulence. Appl. Sci. Res. 53, 357–374.
Peterson, F.B., 1972. Hydrodynamic cavitation and some considerations of the influence of free gas content. In: Proceedings of the 9th Symposium on Naval Hydrodynamics. Paris, France.
Rood, E.P., 1991. Review – mechanisms of cavitation inception. J. Fluids Eng. 113 (2), 163–175.
Saito, Y., Takami, R., Nakamori, I., Ikohagi, T., 2007. Numerical analysis of unsteady behavior of cloud cavitation around a NACA0015 foil. Comput. Mech. 40, 85–96.
Salvatore, F., Streckwall, H., van Terwisga, T., 2009. Propeller cavitation modelling by CFD-results from the VIRTUE 2008 Rome workshop. In: Proceedings of the First International Symposium on Marine Propulsors.
Schlatter, P., Örlü, R., 2010. Assessment of direct numerical simulation data of turbulent boundary layers. J. Fluid Mech. 659, 116–126.
Shams, E., Finn, J., Apte, S.V., 2011. A numerical scheme for Euler–Lagrange simulation of bubbly flows in complex systems. Internat. J. Numer. Methods Fluids 67 (12), 1865–1898.
Truesdell, C., 1954. The Kinematics of Vorticity, first ed. Indiana University Press.